The Kinetics of H_2O Vapor Condensation and Evaporation on Different Types of Ice in the Range 130−210 K†

Pascal Pratte, Hubert van den Bergh, and Michel J. Rossi*

Ecole Polytechnique Fédérale de Lausanne (EPFL), Laboratoire de Pollution Atmosphérique et sol (LPAS), Bât CH H5, station 6, CH-1015 Lausanne, Switzerland

Received: July 19, 2005; In Final Form: September 8, 2005

The kinetics of condensation (k_c) and the evaporation flux (J_{ev}) of H_2O on ice were studied in the range 130−210 K using pulsed-valve and steady-state techniques in a low-pressure flow reactor. The uptake coefficient γ was measured for different types of ice, namely, condensed (C), bulk (B), single crystal (SC), snow (S), and cubic ice (K). The negative temperature dependence of γ for C, B, SC, and S ice reveals a precursor-mediated adsorption/desorption process in agreement with the proposal of Davy and Somorjai.[1] The non-Arrhenius behavior of the rate of condensation, k_c, manifests itself in a discontinuity in the range 170−190 K depending on the type of ice and is consistent with the precursor model. The average of the energy of sublimation $\Delta H_S°$ is (12.0 ± 1.4) kcal/mol for C, B, S, and SC ice and is identical within experimental uncertainty between 136 and 210 K. The same is true for the entropy of sublimation ΔS_S. In contrast, both γ and the evaporative flux J_{ev} are significantly different for different ices. In the range 130−210 K, J_{ev} of H_2O ice was significantly smaller than the maximum theoretically allowed value. This corroborates γ values significantly smaller than unity in that T range. On the basis of the present kinetic parameters, the time to complete evaporation of a small ice particle of radius 1 μm is approximately a factor of 5 larger than that previously thought.

1. Introduction

Although only 10^{-5} of the global abundance of H_2O is present in the atmosphere, it is the most important greenhouse gas that primarily controls the global radiation budget on our planet. Owing in a large part to the positive radiative forcing of water vapor (H_2O(g)) the greenhouse effect keeps the average global temperature well over the melting point of H_2O and thus enables life on earth. Evaporation from oceans, lakes, and rivers is balanced by precipitation over land and sea leading to an average residence time of 10 days for H_2O(g) in the atmosphere.[2] This means that the mixing of H_2O vapor on a global scale is incomplete which leads to a large degree of spatial inhomogeneity of atmospheric H_2O(g) and consequently to a high local variability of H_2O(g).[3−5] It has been known for some time that a significant fraction of the free troposphere is either under- or supersaturated with respect to H_2O(g) depending on meteorological conditions or long-range transport phenomena.[4,6−8] This fact and the large temperature fluctuations that accompany the "weather" in the free troposphere underline the importance of H_2O(g) evaporation and condensation processes in the atmosphere both of which tend to restore thermodynamic equilibrium of H_2O(g).

The present work focuses on the kinetics of condensation and evaporation of H_2O on ice at low temperatures characteristic of the tropopause region, that is, in the upper troposphere (UT) and lower stratosphere (LS). Ice occurs as cirrus cloud or aviation contrail particles which have a positive radiative forcing leading to global warming in contrast to warm clouds at lower altitudes that mostly consist of liquid water droplets and that are approximately neutral with respect to global radiative forcing.[9] Approximately a quarter of all cirrus clouds at any given time are visible by the naked eye because they have a significant optical thickness whereas the remaining 75% of the cirrus are subvisible.[10] The cirrus ice particles typically have radii of 10−20 μm[11−13] in the tropical UT and often lead to local increases of positive radiative forcing.[14] Cirrus clouds are particularly prevalent in the cold tropical tropopause region to the extent of 50% of the atmosphere whereas their abundance decreases to approximately 25% at midlatitudes as indicated above.[15]

In addition to their known climate effect, these cirrus and contrail[16] ice particles also have an effect on the composition of the corresponding atmospheric strata as they not only support adsorption and desorption processes but may also contribute to the occurrence of heterogeneous chemical processes of atmospheric trace gases on ice. On the basis of a modeling study of heterogeneous chemistry in the midlatitude UT, a benchmark minimum reaction time of 20 min has been obtained that led to a significant perturbation of the UT composition.[15,17] This also means that a minimum ice particle lifetime of the same order had to be postulated, ice being the seat of the investigated heterogeneous processes. One of the most important ice particle characteristics is its evaporative lifetime in an atmosphere undersaturated with H_2O(g) vapor which may be calculated at any relative humidity of H_2O vapor if the basic chemical kinetics of equilibrium 1 involving the condensation rate constant (k_c/s^{-1}) and the evaporation rate (R_{ev}/molecules s^{-1} cm^{-3}) is known

$$H_2O(g) \leftrightarrow H_2O(ice) \qquad (k_c, R_{ev}) \tag{1}$$

If the uptake coefficient, γ, of H_2O(g) on ice derived from k_c is assumed to be equal to unity, as has frequently been done, the cirrus ice particle lifetime is significantly less than 10 min at

† Part of the special issue "Jürgen Troe Festschrift".

* Corresponding author. E-mail: michel.rossi@epfl.ch.

10.1021/jp053974s CCC: $33.50
Published on Web 10/15/2005

temperatures (T) and relative humidities of the UT; heterogeneous chemistry does not have a chance to occur under those conditions. Conversely, for γ significantly less than unity, as obtained in the present work, heterogeneous chemistry may perturb the atmospheric composition. Therefore, it is of utmost importance to obtain reliable kinetic parameters on both the rate constant of condensation (k_c) and the rate of evaporation (F_{ev}/molecule s^{-1}) as a function of temperature in the range of interest. The morphology of thermodynamically stable ice I_h may considerably vary depending on a suite of parameters that control the growth processes of atmospheric ice.[18] Although the above-mentioned kinetics may depend on the ice morphology, very little information from the field is available concerning the type of ice particles prevalent in cirrus clouds. Laboratory studies have revealed that liquid droplets frozen at $T > 180$ K consist of I_h.[19,20] Recent laboratory reports even estimate the probability of finding metastable cubic ice (I_c) in the atmosphere, whose occurrence has been suspected in the past.[21−23]

Because most of the literature reports the kinetics of H_2O vapor with ice condensed from the vapor phase (condensed or C ice), the present work emphasizes this type of ice in order to provide a solid basis for quantitative comparison. The strategy adopted in the present work was to study the kinetics of H_2O(g) condensation and evaporation on many different types of ices that we could generate in the laboratory under well-defined and reproducible conditions in order to learn more about the variability of the kinetic results as well as on the underpinning molecular mechanism. Several workers have oriented their efforts toward the measurement of the kinetics of H_2O(g) both over liquid water and over ice in terms of γ as well as the evaporation rate R_{ev} or flux J_{ev} as a function of T.[24−28] Experimental values of γ range from 0.03 to 1.0 using different experimental techniques such as measurements of weight, ice crystal growth, droplet radial growth, vapor loss, liquid film growth, and IR absorption in the range 138−293 K.[24−27,29−32] The large variability in γ at any given temperature suggests the potential importance of controlling the many ice growth parameters in addition to allowing for potential experimental artifacts. We report the fundamental kinetics of the H_2O(g) interaction with different types of ices generated in the laboratory under reproducible conditions using both pulsed valve in real-time as well as steady-state methods that enable the separate measurement of both the condensation and evaporation process displayed in reaction 1. The separate determination of both rates enabled the measurement of the equilibrium vapor pressure, P_{eq}, which serves as a powerful thermodynamic constraint for checking the internal consistency of the kinetics of the T-range of interest in thermochemical closure.

2. Experimental Setup

The experiments have been performed in a Teflon-coated Knudsen flow reactor equipped with molecular-beam-sampling electron-impact mass spectrometry (MS). A detailed description of this technique has been given elsewhere.[33] Two types of measurements have been performed: continuous flow and pulsed admission experiments (PV). The PV experiments correspond to a transient supersaturation of H_2O(g) over ice using a pulsed solenoid valve through which short pulses of H_2O molecules of several millisecond duration have been injected into the flow reactor. Each experiment has been performed in duplicate, that is a reference and a reactive experiment. The former yields the MS signal decay of H_2O(g) when the sample compartment is isolated from the flow reactor, whereas the latter monitors the decay in the presence of the ice substrate. The decay rate in the absence of the ice sample is given by the measured escape rate constant k_{esc} at which H_2O(g) molecules effuse out of the reactor and is related to the gas-phase lifetime, τ_g, of H_2O(g) through the relation $\tau_g = 1/k_{esc}$. This represents the reference experiment against which the reactive decay of the MS signal in the presence of ice is measured. The measurement of k_{esc} was repeated 10 times for each orifice in order to obtain its standard deviation. The evaporation and condensation of H_2O(g)/H_2O(ice) on the ice substrate are competing with k_{esc} as displayed in reaction 2. In the presence of ice the measured pulse decay constant k_{dec} is the sum of the condensation k_c and escape rate constant k_{esc}, namely, $k_{dec} = k_c + k_{esc}$. From the measured decay constant k_{dec}, k_c is directly accessible using the measured value of k_{esc} that is displayed in Table 1.

TABLE 1: Experimental Parameters

reactor volume (V, cm^3)				1830
cryogenic sample surface (A_S, cm^2)				17.65
collision frequency of H_2O on sample surface (ω) at 300 K (s^{-1})				143
escape aperture diameter (mm)	14	8	4	1
escape rate constant (s^{-1})	7.1 ± 0.2	3.1 ± 0.3	0.8 ± 0.1	0.05 ± 0.01

$$\xleftarrow{k_{esc}} H_2O(g) \underset{R_{ev}}{\overset{k_c}{\rightleftharpoons}} H_2O(ice) \qquad (2)$$

The largest exit aperture of 14 mm diameter has been used in view of the fast rates of H_2O(g) uptake on ice. Typical doses of H_2O(g) were in the range $10^{15}-10^{17}$ ($\pm 4 \times 10^{14}$ molecule per pulse) or between 0.05 and 5 monolayers of H_2O-ice based on the geometric surface area S of the ice sample. The upper limiting temperature of the ice was 205 K beyond which evaporation led to a H_2O(g) partial pressure whose mean free path violated the Knudsen flow condition and which reduced the value of k_{esc} in comparison with the value measured under molecular flow conditions. Nevertheless, k_c was obtained in the T range 205−210 K using the measured values of k_{esc}.

We have directly measured the rate k_c together with the steady-state flow rate F_{ss} of H_2O(g) escaping the reactor in order to evaluate the evaporation rate $R_{ev} = F_{ev}/V$ and flux $J_{ev} = R_{ev}(S/V)^{-1}$, where V is the volume of the reactor. A typical experiment is displayed in Figure 1 where the H_2O(g) reference pulse is fired into the reactor with the sample compartment closed (Figure 1a, plunger lowered), whereas the reactive pulse is admitted into the flow reactor with the sample compartment open (Figure 1b, plunger lifted). At steady-state conditions and open sample compartment the rate of evaporation (F_{ev}), condensation $k_c[H_2O(g)]V$, and escape $k_{esc}[H_2O(g)]V$ of H_2O(g) compete as expressed in the following balance of rates

$$\frac{dN}{dt} = F_{ev} - k_c N - k_{esc} N = 0 \text{ [molecules } s^{-1}] \qquad (3)$$

where N is the total number of H_2O(g) molecules present in the reactor and is given by $[H_2O(g)]V$.

The dimensionless uptake coefficient γ was calculated following eq 4

$$\gamma = \frac{k_c}{\omega} \qquad (4)$$

where ω (s^{-1}) is the collision frequency of the average H_2O(g) molecule with the geometric sample surface S at 300 K and is displayed in Table 1.

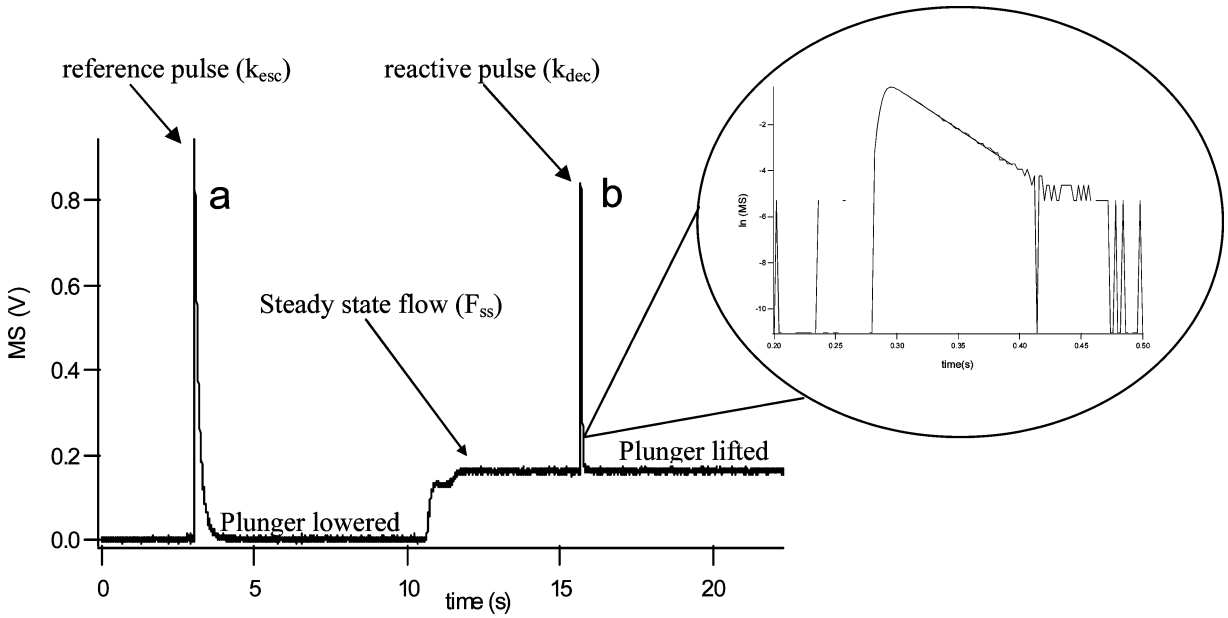

Figure 1. Typical pulsed valve experiment of H_2O(g) interacting with bulk (B) ice at 200 K. The H_2O(g) dose was 5.0×10^{16} molecules and corresponds approximately to 2.5 formal monolayers. Pulses a and b represent the reference and reactive pulses, respectively. The inset shows the semilogarithmic plot of the reactive decay given by k_{dec}.

Equation 3 yields after rearrangement

$$F_{ev} = F_{SS}\left(1 + \frac{k_c}{k_{esc}}\right) [\text{molecules s}^{-1}] \qquad (5)$$

Equation 5 puts into relation the measured steady-state H_2O(g) flow rate F_{ss} at the calibrated MS signal at *m*/*e* 18 as displayed in Figure 1 with the measured ratio $k_c/k_{esc.}$ As discussed above, k_c was obtained from the exponential decay of a reactive H_2O(g) pulse monitored at *m*/*e* 18 as displayed in the insert of Figure 1. In the present experiments, k_c values of typically five separate pulsed dosing experiments at a given value of T were averaged in order to obtain an average value of F_{ev}. The temperature difference between the flow reactor (ambient T) and the ice substrate (low T) affects the magnitude of k_c such that a small correction for the thermal transpiration effect has to be applied. However, the correction of the ratio k_c/k_{esc} in eq 5 cancels out[34] and the resulting F_{ev} only depends on the temperature of the ice substrate. In addition, we have validated the transient supersaturation PV experiment by additional steady-state experiments which gave identical results. Further details may be found in Appendix A.

2.1. MS Signal Calibration Procedure for H_2O Vapor. The calibration of the MS signal of H_2O(g) at *m*/*e* 18 has been performed by freezing a water droplet of (9.00 ± 0.05) mg mass (Mettler Toledo, AE 240 balance) deposited on the cryogenic support device described elsewhere[33] using a calibrated syringe. The mass of the water droplet was determined gravimetrically, and the temperature of the supported droplet rapidly decreased to 160 K. Gradually, the temperature of the droplet was increased while the H_2O(g) flow rate was monitored at *m*/*e* 18 as a function of time. The MS signal returned to the baseline after complete evaporation of the deposited drop after typically 30 min and at 230 K. The resulting area under the MS signal was proportional to the total number of molecules in the droplet and led to the desired calibration factor whose average is associated with a standard deviation of 5%. A blank without depositing a water droplet on the gold-plated cryogenic support resulted in deposition of 0.1% of the mass of the deposited water droplet, H_2O(l).

2.2 Correction for Molecular Diffusion. Pulsed valve experiments tend to underestimate the value of k_c at large values compared to steady-state experiments.[35] For a fast reaction measured in real time, a systematic bias is introduced when the H_2O(g) density is depleted close to the reactive ice sample on a time scale shorter than the characteristic transit time at molecular flow conditions. To correct k_c for the diffusion limitation, we interpolated the curve of Fenter et al.[35] that correlates the measured value of k_c from PV experiments with k_c obtained from the true value of γ at steady state. This correction is important for measured k_c values larger than 20 s^{-1} which led to a correction of $<5\%$. The correction to k_c that was obtained using the PV becomes increasingly important when k_c tends toward ω (Table 1).

2.3. Preparation of Ice Samples. The samples have been prepared in situ in the range 130−210 K using the cryogenic support whose temperature was regulated by a series 900 EUROTHERM temperature controller. Five different types of ice samples have been investigated in order to measure the kinetics of H_2O(g) condensation as a function of temperature for different doses of H_2O(g). Each ice sample was prepared by using degassed bidistilled water (18.2 MΩ).

Bulk ice (B) was prepared by pouring 5 mL of degassed bidistilled water into the cryogenic support and lowering the support temperature at a rate of 0.2 K s^{-1}. At 240 K the ice was held at this temperature for 20 min in order to avoid the buildup of stress in the sample. Subsequently, the ice was cooled to a temperature in the range between 160 and 210 K at a rate of 0.2 K s^{-1}. As displayed in Figure 2a, a typical B ice sample appears white due to its rough surface and light scattering.

Condensed (C) ice is prepared from the condensation of gas-phase H_2O(g) onto the cryogenic support held at 180 K in order to form hexagonal ice.[36] Many parameters may be varied in the preparation of C ice, among which the H_2O(g) flow rate, the residence time of H_2O(g), and the temperature of deposition. In the present experiments, we have varied the flow rate and the residence time in order to change the water concentration, [H_2O(g)], in the reactor. Three concentrations were used to form C ice, leading to C_1, C_2, and C_3 ice. As an example taken from

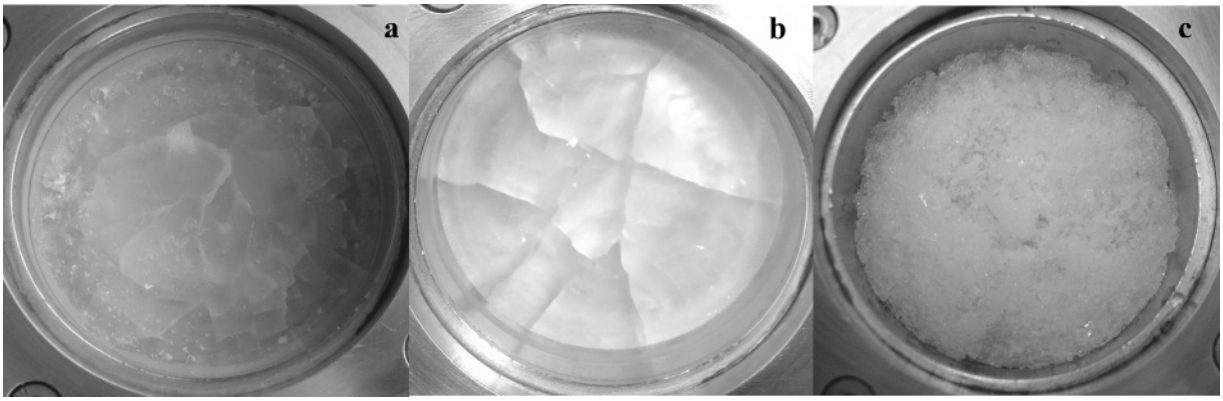

Figure 2. Samples of B ice (a), SC ice (b), and S ice (c) prepared in the 4.74 cm diameter cryogenic sample support. The photograph was taken at ambient temperature.

TABLE 2: H_2O Vapor Deposition Parameters for Condensed (C) Ice Samples

type of ice	deposition time (min)	deposition temp (K)	thickness (μm)	[H_2O] (molecules cm^{-3})	escape aperture diameter (mm)	condensation flow $F_{in} - F_{out}$ ($\pm 5 \times 10^{13}$ molecules s^{-1})	initial flow rate F_n ($\pm 5 \times 10^{13}$ molecules s^{-1})
C_1	50	180	2	$(7.1 \pm 0.5) \times 10^{12}$	8	3×10^{16}	4.1×10^{16}
C_2	10	180	4	$(7.1 \pm 0.5) \times 10^{13}$	8	3×10^{17}	3.9×10^{17}
C_3	10	180	5	$(4.4 \pm 0.9) \times 10^{15}$	1	4×10^{17}	4.0×10^{17}
K (cubic)	10	130	5	$(4.4 \pm 0.9) \times 10^{15}$	1	4×10^{17}	4.2×10^{17}

Table 2 we have used the 8 mm aperture and an initial $H_2O(g)$ flow rate of 3.9×10^{17} molecules s^{-1}, leading to [$H_2O(g)$] = $(7.1 \pm 0.5) \times 10^{13}$ molecule cm^{-3}. In this case, 75% of the initial $H_2O(g)$ flow rate F_{in} is lost from the gas phase to form C_2 ice at 180 K. The deposition was performed for 10 min in order to form a 4 μm thick ice film of C_2 ice ($0.75 \times 3.9 \times 10^{17}$ molecules s^{-1} $\times$ 600 s)/(1.0×10^{15} molecules cm^{-2} $\times$ 17.65 cm^2). The parameters used to form C ice type are summarized in Table 2.

The deposition parameters used to generate cubic (K) ice are the same as for C_3 ice except for the temperature (Table 2). In this case, the temperature of the cryogenic support is lowered to 130 K and ice is formed by introducing $H_2O(g)$ into the reactor for 10 min at a flow rate indicated in Table 2. The uptake kinetics of $H_2O(g)$ is measured at 130 K using the PV technique. Subsequently, the sample previously generated at 130 K was annealed to 150 K for 10 min and cooled back to 130 K for additional uptake measurements. The same procedure was repeated for different annealing temperatures using the same K ice sample, to check for structural changes and their effects on k_c. Fresh K ice presumably consists of a mixture of cubic and hexagonal ice under our experimental conditions.[36]

Single crystal (SC) ice has been obtained by slowly freezing 5 mL of liquid degassed bidistilled water at a rate of 1/3 K min^{-1} down to 240 K in order to avoid build up of stress during crystal growth.[37] Subsequently, the ice was cooled to the desired temperature at a rate of 0.2 K s^{-1}. We assume that SC ice possesses a very low surface defect density in agreement with literature reports.[20,36] A typical SC ice sample is transparent and is displayed in Figure 2b. Visual observation of parts a and b of Figure 2 suggests that the surface roughness of B and SC ice is different. Therefore, a quantitative test was performed in order to characterize the surface roughness using the reflection of a He−Ne laser beam (UNIPHASE, 10 mW) oriented at 10° with respect to the surface normal of the cryogenic support. The signals S_B, S_{SC}, and S_{ref} were measured for B, SC ice, and for the bare Au-plated support surface, respectively. The result $1 - S_B/S_{ref} = 64 \pm 18\%$ and $1 - S_{SC}/S_{ref} = 13 \pm 1\%$ is a measure of the scattering efficiency of the ice sample and supports the surface roughness of B ice in comparison to SC ice.

The snow (S) ice sample preparation consisted of preparing ex situ ice samples in humidified N_2 (relative humidity (RH) = 90% at 296 K) at atmospheric pressure and a flow of 1 L min^{-1}. To cover the entire surface of the sample holder (17.65 cm^2) with approximately 2 mm of loosely packed snow, a deposition of at least 1 h was required. A typical S ice sample is displayed in Figure 2c.

In the following, the units kcal/mol and Torr have been used. One multiplies the energies (kcal/mol) and the pressure (Torr) by 4.184 and 133.33, respectively, to obtain the SI units kJ/mol and Pa.

3. Results and Discussion

3.1. Rate Law for the Condensation of H_2O on Ice. To determine whether the rate of $H_2O(g)$ condensation on B ice is first order in [$H_2O(g)$], the dependence of k_c or γ on the $H_2O(g)$ dose must be measured. Figure ESI-1 displays the uptake coefficient γ of $H_2O(g)$ interacting with B ice as a function of dose at different temperatures. We conclude that the kinetics of $H_2O(g)$ condensation on B ice is independent of [$H_2O(g)$] and thus confirm the first-order kinetics of $H_2O(g)$ condensation on B ice over the dose range 10^{15} to 3.0×10^{17} molecules.

Similar experiments were performed to test the rate law for $H_2O(g)$ uptake for C, SC, S, and K ice. Figure 3 displays data on $\gamma(T)$ measured on C_2 ice for small (5.0×10^{15} molecules/pulse) and large doses (2.0×10^{17} molecules/pulse) as a function of T with B ice plotted as a reference. We conclude that there is no significant difference between large and small dose data which confirms that uptake of $H_2O(g)$ on C_2 ice follows a first-order rate law as was the case for B ice.

By changing the sample preparation conditions, the surface structure of B and C ice may change and may possibly lead to changes in $\gamma(T)$. If the rate at which B ice is frozen is lowered, a low defect density ice (SC) is formed which may have different kinetic properties compared to B ice.[36] Figure 4 shows that γ

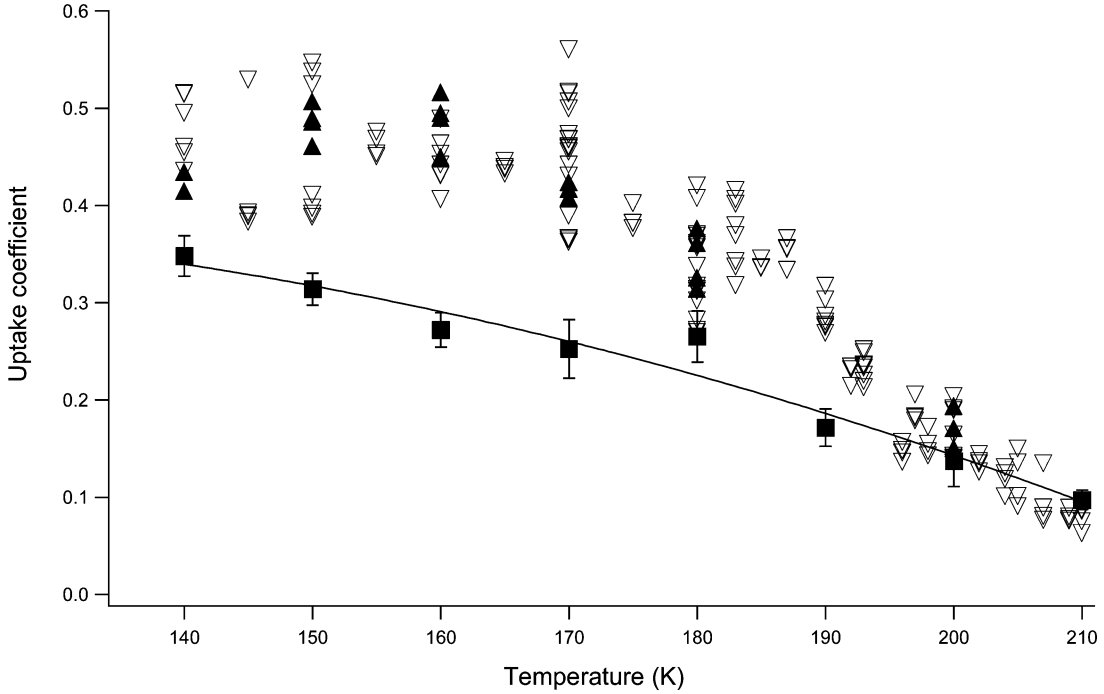

Figure 3. Uptake coefficient γ for C_2 ice displayed for two different doses resulting from PV experiments: the filled (▲) and empty (▽) triangle data correspond to doses of 5.0×10^{15} and 5.0×10^{16} molecules/pulse, respectively. γ for B (■) ice is plotted as a reference.

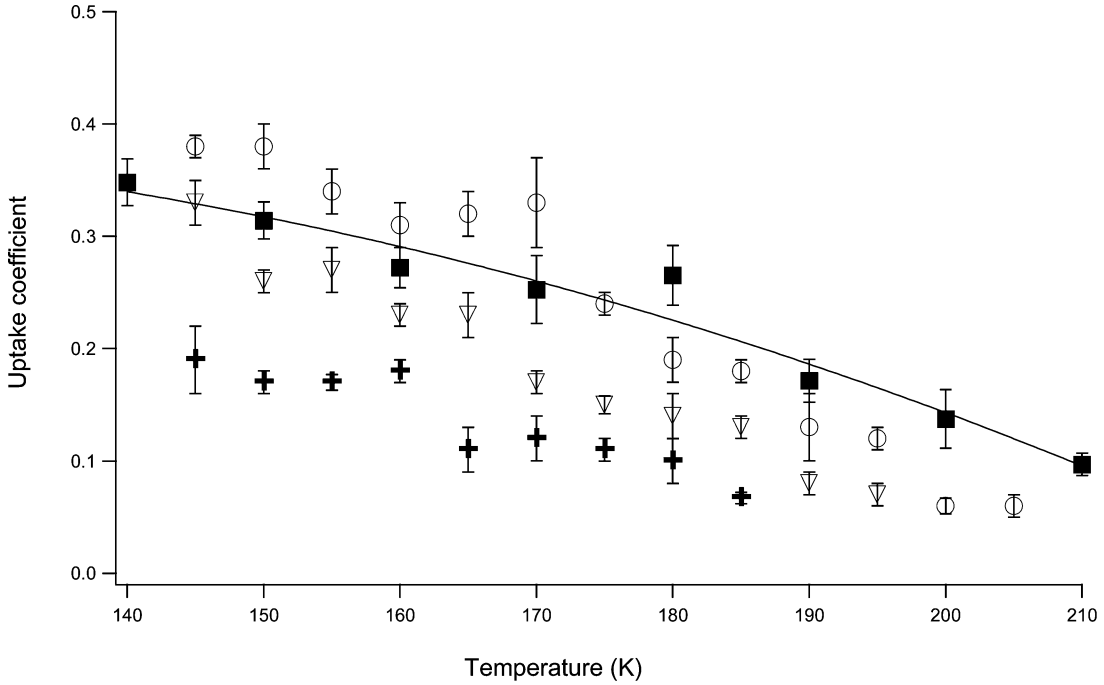

Figure 4. Uptake coefficient γ for SC ice plotted as a function of temperature for three different doses, namely, 1.0×10^{15} (+), 9.0×10^{15} (▽), and 5.0×10^{16} (○) molecules/pulse. B ice (■) data are presented as a reference.

on SC ice is a function of T and of the dose when using three significantly different doses. In fact, there is a factor of 2 difference in γ between large (5.0×10^{16} molecules/pulse) and small doses (1.0×10^{15} molecules/pulse) for H_2O(g) uptake on SC ice. SC ice is a case where the kinetics of H_2O(g) condensation does not seem to follow a first-order rate law. The present work shows that $\gamma(T)$ is larger by up to a factor of 2 when the dose or instantaneous concentration increases by a factor of 50 in the range 140−210 K.

K ice is formed like C_3 ice except for the temperature of deposition (Table 2). Using three different doses differing by a factor of 50, we have observed that γ is independent of dose at 130 K as displayed in Figure 5. We conclude that H_2O(g) adsorption for cubic ice follows a first-order rate law.

S ice was made by slow growth of ice crystals under 1 atm of N_2. The kinetics was measured over the temperature range 136−200 K using three doses varying by a factor of 30. The results are displayed in Figure 6 which shows that there is no significant difference in γ for large (8.0×10^{16} molecules/pulse) and small doses (3.0×10^{15} molecules/pulse). In fact, the difference between the mean of the large and small dose is about 20%, which corresponds to the uncertainty of the data. Consequently, we conclude that the uptake of H_2O(g) on S ice is first order in H_2O.

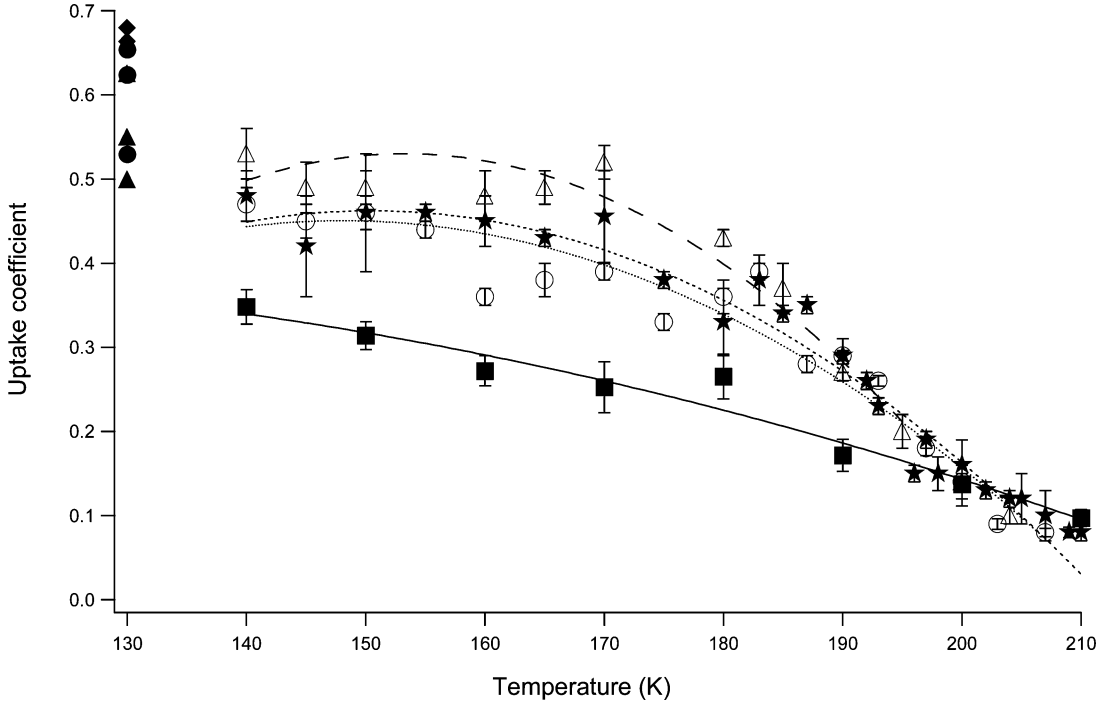

Figure 5. Uptake coefficient γ plotted as a function of temperature for three different C ice samples, namely, C_1 (○), C_2 (★), and C_3 (△) and using a H_2O(g) dose of 5×10^{16} molecules/pulse. The C_x deposition parameters are described in Table 2; γ values for B (■) and K ice are displayed as a reference. Three different doses were used to measure γ of K ice: 1.5×10^{15} (●), 9.0×10^{15} (♦), and 8.0×10^{16} (▲) molecules/pulse. The doses used on B are comprised in the range 10^{15} to 3×10^{17} molecules and the measured kinetic of condensation was averaged over doses (Figure ESI-1).

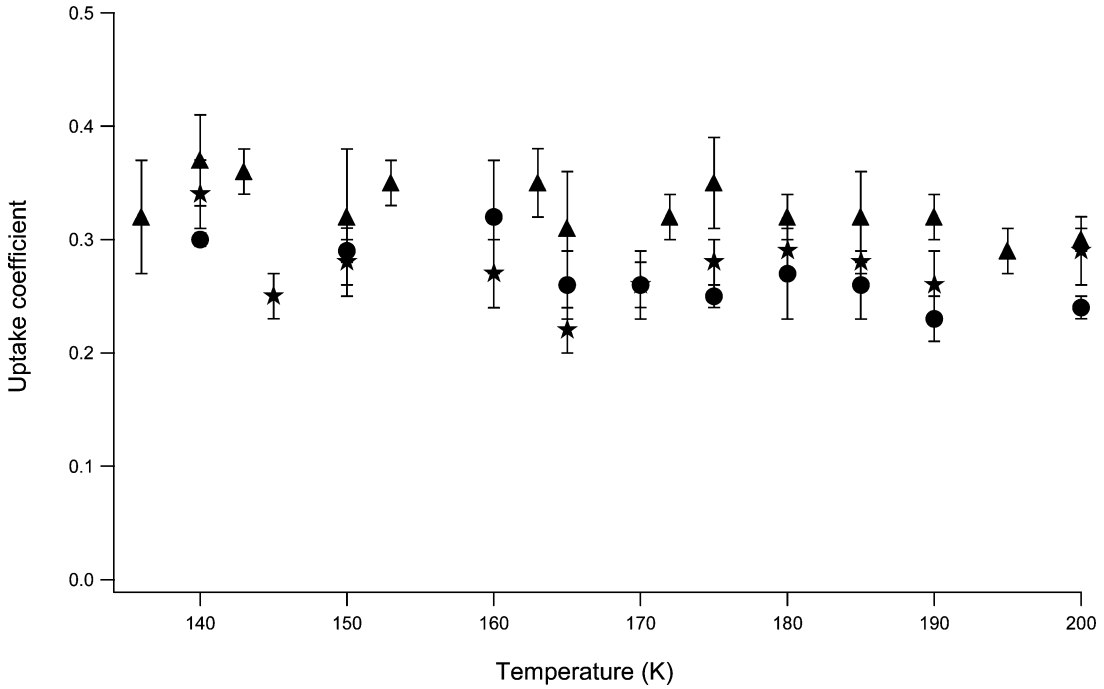

Figure 6. Uptake coefficient γ of S ice as a function of T. The different symbols compared γ values obtained at different doses of H_2O(g): 3.0×10^{15} (★), 9.0×10^{15} (●), and 8.0×10^{16} (▲) molecules/pulse.

In summary, the uptake of H_2O(g) on C, B, K, and S is first order in H_2O while γ for SC seems to depend on the dose over a range of a factor of 30−50. Depending on the ice deposition/formation protocol, one must determine the rate law of H_2O(g) uptake on ice if one wants to extrapolate to low supersaturations occurring in the atmosphere. Except for SC ice the use of γ is justified as a transferable parameter of ice growth over a temperature range characteristic of the UT/LS.

3.2. The Dependence of γ on Temperature and H_2O Deposition Rate for C Ice. Typically, the limiting values of γ for uptake of H_2O(g) on C_2 ice lie between 0.48 ± 0.04 and 0.08 ± 0.03 at 140 and 210 K (Table 3), respectively, and are plotted as a function of T in Figure 5. The data clearly show that γ for C_2 ice has a negative temperature dependence which is in agreement with a complex mechanism that implies one or more precursor species as has been found before.[38,39] This result is also in agreement with Haynes et al.[40] who confirm the negative temperature dependence first found by Davy and Somorjai[1] in the range 183−233 K together with the fact that $\gamma < 1.0$ at $T > 130$ K. However, the same workers[40]

TABLE 3: Range of γ for Different Types of Ice

type of ice[a]	γ	temp (K)
B	0.35 ± 0.02 to 0.10 ± 0.02	140−210
C_2	0.48 ± 0.04 to 0.08 ± 0.03	140−210
SC (L)	0.38 ± 0.01 to 0.06 ± 0.01	145−205
SC (M)	0.33 ± 0.02 to 0.08 ± 0.01	145−195
SC (S)	0.20 ± 0.03 to 0.10 ± 0.02	145−185
S	0.32 ± 0.05 to 0.29 ± 0.02	136−200
K	0.64 ± 0.05	130

[a] L, M, and S are large, medium, and small doses corresponding to 5.0×10^{16}, 9.0×10^{15}, and 1.0×10^{15} molecules/pulse.

unfortunately revoked their results later by setting $\gamma = 1.0$ across the entire temperature range of 20−185 K in order to determine the optical constants for the used ice films.[41]

The way C ice is formed may potentially change the kinetic properties of the ice surface. For that reason k_c was measured for three different [H_2O(g)] (C_1, C_2, C_3) differing by a factor of 600 and displayed in Table 2. The kinetic results are displayed in Figure 5 where γ is plotted as a function of temperature for C_1, C_2, and C_3 ices. The results show that γ for C ice increases somewhat with the H_2O(g) concentration varied by a factor of 600. Taking the two extreme cases C_3 vs C_1 ice, the former presents a γ value approximately 10−30% larger for $T < 190$ K compared to C_1. However, we do not find a significant dependence of γ on the H_2O(g) deposition rate for C ice at $T > 190$ K as all values seem to merge to a common value as displayed in Figure 5. This may be an indication that the mechanism of H_2O(g) uptake may change around 190 K, as will be discussed below.

Haynes et al.[40] have performed measurements of γ by isothermal evaporation of C ice in the range 20−185 K. They obtained $\gamma = 0.75$ and 0.69 at 160 and 185 K, respectively, in contrast to the present values for C_1 ice which lie between $\gamma = 0.36 \pm 0.04$ at 160 K and $\gamma = 0.32 \pm 0.06$ at 185 K. It is likely that the vapor deposition conditions used by Haynes et al.[40] were closer to C_1 than to C_3 deposition conditions (Table 2). This discrepancy of approximately a factor of 2 in γ may perhaps be explained by the fact that γ depends on the way the ice sample was prepared. In fact, they measured γ between 20 and 185 K on ice condensed from H_2O(g) at a total pressure ranging from 3.3×10^{-6} to 6.6×10^{-5} Torr. In contrast, in this work C_1 ice was deposited at 180 K at a pressure of $2.20 \pm 0.15 \times 10^{-4}$ Torr which is higher by at least a factor of 3. This and the different temperature of deposition may lead to structural differences and therefore to changes of reactivity toward H_2O(g) vapor. Delval and Rossi[42] measured a γ value of 0.38 and 0.12 at 185 and 207 K, respectively, on C ice condensed at 190 K at a H_2O(g) flux of 1.0×10^{17} molecules s^{-1} cm^{-2} compared to 1.7×10^{15} molecules s^{-1} cm^{-2} of H_2O-(g) in the present study. Within the uncertainty of the present measurement, namely, $\gamma = 0.32 \pm 0.06$ and 0.08 ± 0.05 at 185 and 207 K, respectively, γ for C_1 ice is in agreement with Delval et al.[42] Moreover, the agreement improves for C_3 ice resulting in $\gamma = 0.37 \pm 0.06$ and 0.10 ± 0.04 at 185 and 207 K, respectively, at a deposition flux of 2.3×10^{16} molecules s^{-1} cm^{-2}, which approaches the H_2O(g) flux used by Delval et al.[42]

3.3. The Evaporation Flux (J_{ev}) from C Ice. The evaporation rate, F_{ev}, in molecules s^{-1}, was obtained from eq 5 by measuring k_c and F_{ss} in the same experiment as displayed in Figure 1. As an example, the evaporative flux, J_{ev} in molecules cm^{-2} s^{-1}, is displayed in Figure 7 and Table ESI-1. The solid line corresponds to the maximum theoretical value, J_{ev}^{max}, that is obtained by setting γ to unity using the vapor pressure P_{eq} of Marti and Mauersberger[43] that has been extrapolated for $T < 165$ K. Delval and Rossi have recently measured J_{ev} using a microbalance technique in a stirred flow reactor at temperatures ranging from 172 to 203 K.[42] Their results match the present J_{ev} data for C_2 ice in this interval within 25%. Moreover, they have measured J_{ev} at $T > 196$ K using a stirred flow reactor technique[34] that agrees with the present data to within 10%. The results of Smith et al.[44] and Haynes et al.[40] are in very good agreement with the present values of J_{ev} for C_2 ice and with the microbalance data of Delval and Rossi[42] to within 35% which is remarkable in view of the different experimental techniques invoked. J_{ev} measured at 170 K by Fraser et al.[45] is a factor of 2 larger than the present data for C_2 ice. More serious is the discrepancy in J_{ev} between the data of Davy and Somorjai[1] and the present values: the former measure J_{ev} values that are larger by roughly a factor of 10 in the range 186−218 K. In contrast, J_{ev} measured by Sack and Baragiola[46] significantly exceeds the maximum evaporation flux J_{ev}^{max} in the range 135−170 K. At 150 and 170 K, J_{ev} exceeds J_{ev}^{max} by 250% and 30%, respectively, for no apparent reason. In summary, although J_{ev} of C ice depends somewhat on the used H_2O(g) deposition rate for the generation of C ice as measured from the corresponding γ values (Figure 5), all J_{ev} values are significantly smaller than J_{ev}^{max} and imply a γ value significantly lower than unity between 140 and 240 K. The discrepancy between J_{ev}^{max} and J_{ev} thereby increases with T.

3.4. The Dependence of γ on Temperature for Other Types of Ice. The γ value for B ice varies between 0.35 ± 0.02 and 0.10 ± 0.02 in the range 140−210 K as displayed in Table 3. Like for C_2 ice, γ of H_2O(g) interacting with B ice is significantly lower than unity and Figure 3 displays the measured γ values for B and C_2 ice at different temperatures. Interestingly, γ for S ice does not change significantly with T as displayed in Figure 6 for three different doses. Table 3 shows that γ lies between 0.32 ± 0.05 and 0.29 ± 0.02 in the range 136−200 K in agreement with Chaix et al.[38] who observed the same weak dependence of k_c on T in the range 140−220 K. SC ice is a special case because k_c does not follow a first-order rate law as discussed above (Figure 4). The γ value changes from 0.38 ± 0.01 to 0.057 ± 0.007 for a large dose of 5.0×10^{16} molecules/pulse in going from 145 to 205 K. For a small dose of 1.0×10^{15} molecules/pulse, γ changes from 0.20 ± 0.03 to 0.10 ± 0.02 from 145 to 185 K as displayed in Figure 4 where γ is plotted for three doses as a function of T spanning a factor of 50 in dose. We note from Figure 4 that γ for B ice seems to be higher at $T > 180$ K and lower at $T < 180$ K compared to SC ice for a high dose of 5.0×10^{16} molecules/pulse probing the surface. In contrast, γ measured on SC ice seems to be smaller compared to B ice for medium (9.0×10^{15} molecules/pulse) and low doses (1.0×10^{15} molecules/pulse). The particular case of K ice was studied at $T = 130$ K where k_c is significantly larger than for the other types of ice studied so far. The cubic ice I_c morphology seems to be more reactive toward condensation of H_2O(g) vapor compared to the hexagonal I_h ice structure and leads to an average γ of 0.64 ± 0.05 at 130 K as displayed in Figure 5. The results for K ice confirm that the PV uptake experiment for all types of ice except for K ice is not limited by instrumental parameters. Several pulse decays are plotted in a semilogarithmic fashion as a function of time in Figure 8 in order to show different pulse decay rates for different types of ice at different temperatures. As an example, the pulse decay for fresh K ice at 130 K is larger by a factor of 4 compared to a C_2 ice sample at 200 K. This comparison displays the typical range of variation in k_c for different ice samples. In conclusion,

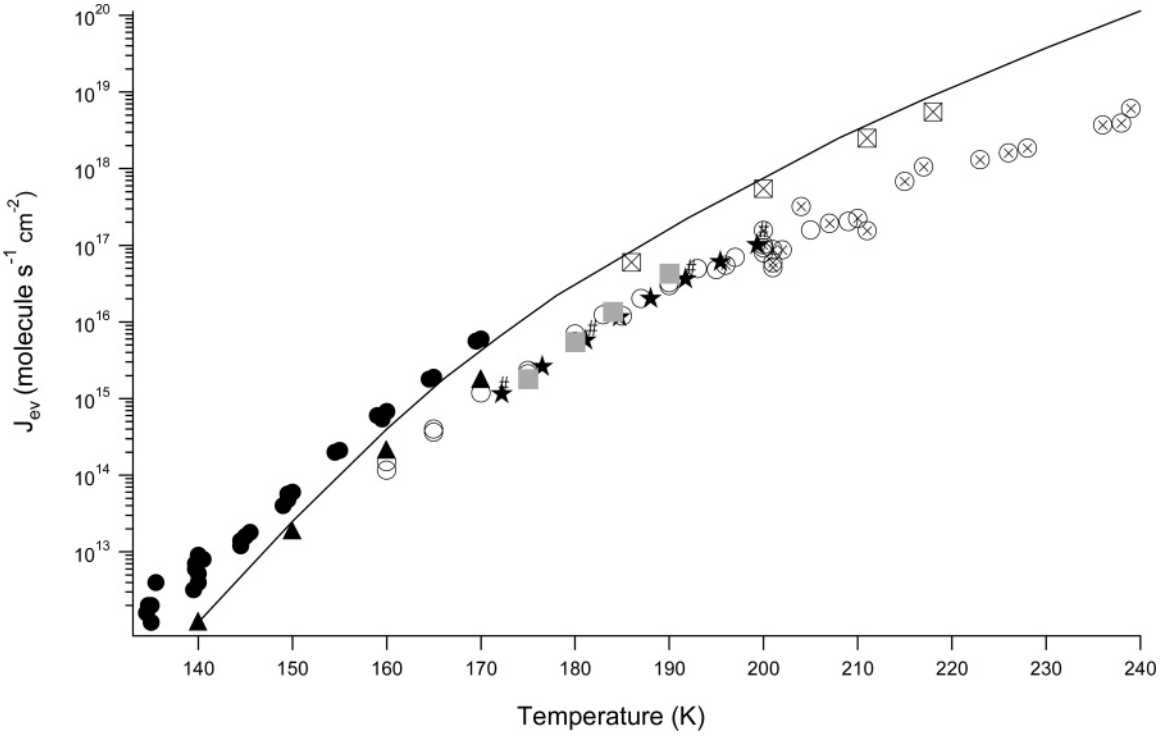

Figure 7. The evaporation flux J_{ev} of H_2O(g) for C_2 ice as a function of T compared to values from the literature in the range 136−240 K: (× inside a square) Davy et al.;[1] (#) Haynes et al.;[40] (▲) Fraser et al.;[45] (shaded square) Smith et al.;[44] (●) Sack at al.;[46] (★) Delval and Rossi[42] (microbalance experiment); (× inside a circle) Delval et al.[34] (stirred flow reactor). This work: (○) pulsed valve experiment on C_2 ice at a dose of 5.0×10^{16} molecules/pulse.

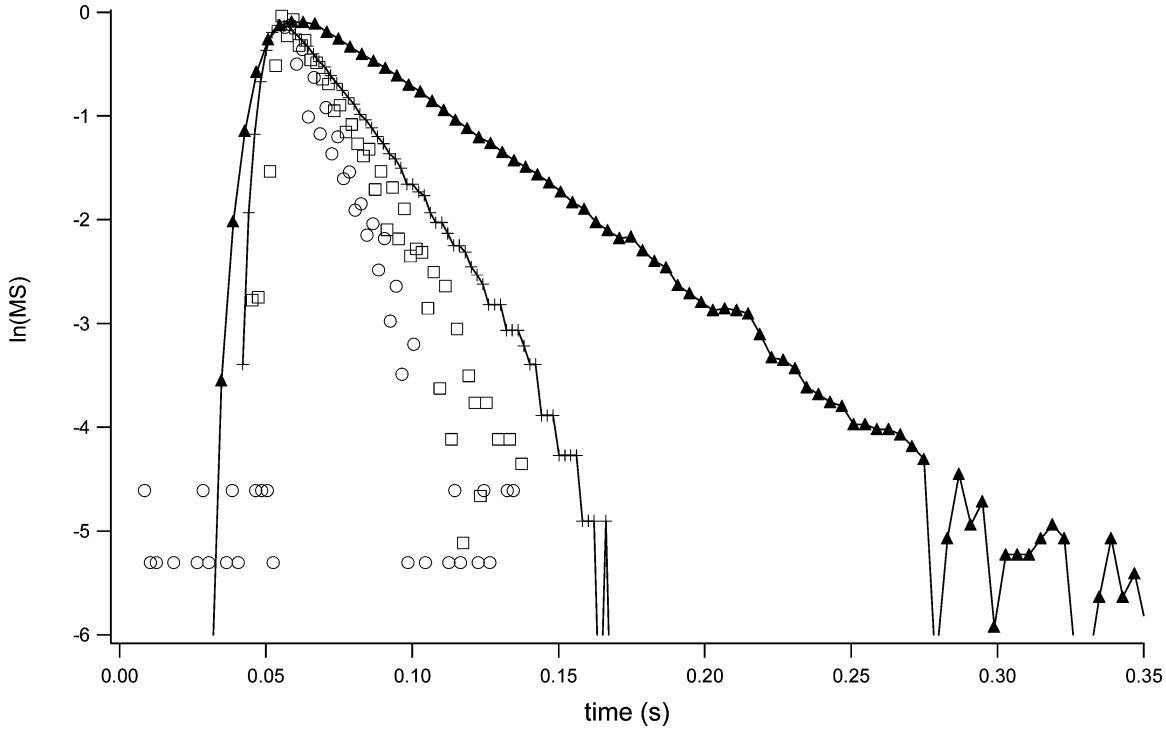

Figure 8. Typical decay kinetics for condensation of H_2O(g) on different ice samples. A dose of 5.0×10^{16} molecules/pulse was used for each of the four pulses. The triangle (▲) corresponds to $k_c = 20$ s^{-1} for C_2 ice at 207 K, the (+) symbol to $k_c = 38$ s^{-1} for B ice at 200 K, and the circle (○) and the square (□) are pulse decays for fresh K ice (68 s^{-1}) at 130 K and for the same K ice sample annealed at 170 K and measured at 130 K (51 s^{-1}), respectively.

γ is significantly different for different types of ice. For $T <$ 185 K, we have the following sequence: γ(K) > γ(C_2) > γ-(SC,L) > γ(B) ≈ γ(S). For $T >$ 185 K, γ(S) > γ(C_2) ≈ γ(B) > γ(SC,L), where L means a large dose of typically 5×10^{16}, compared to a small dose of 1.0×10^{15} molecules/pulse.

3.5. The Evaporation Flux (J_{ev}) for Other Types of Ice. In addition to J_{ev} for C_2 discussed above, we have determined J_{ev} on the other types of ice, namely, for B, SC, and S ice that are displayed in Figure 9 and Tables ESI-2, ESI-3, ESI-4 and ESI-5 as a function of T. Except for K ice, we conclude that C_2

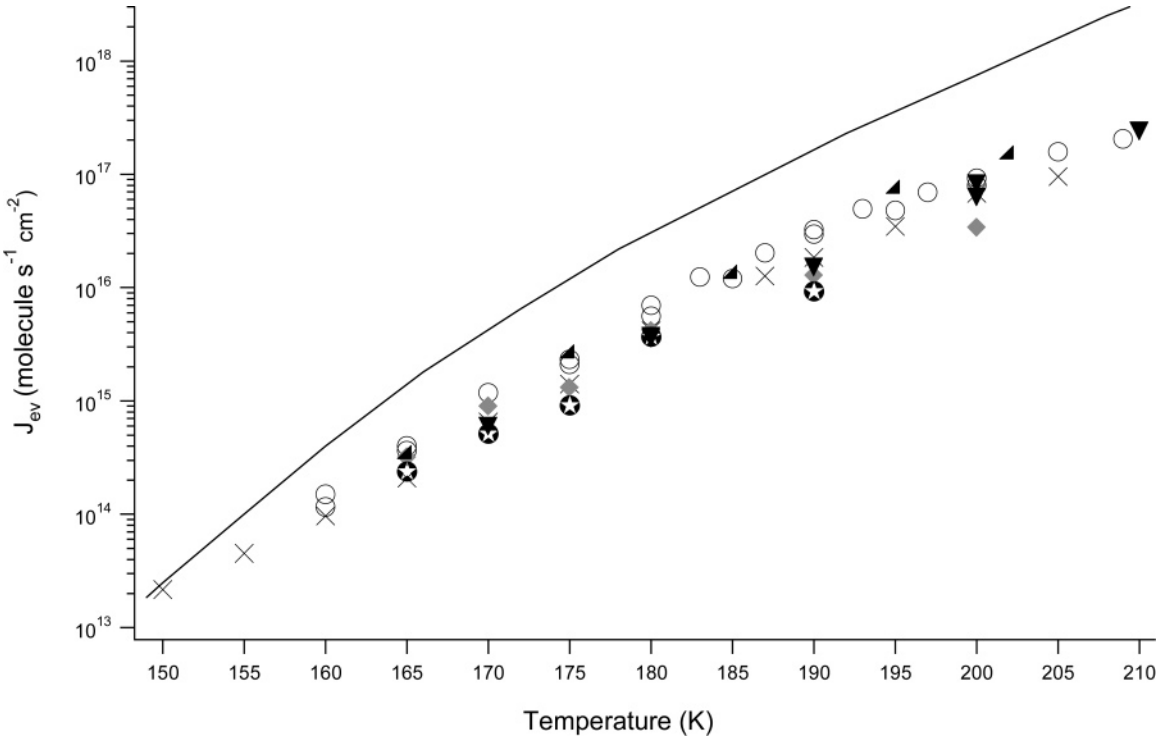

Figure 9. J_{ev} of $H_2O(g)$ as a function of temperature for the different types of ice between 150 and 210 K: (▼) CFM experiment (Appendix A) on B ice; (×) PV experiment on B ice; (○) PV experiment on C_2 ice; (shaded diamond) PV experiment on SC (large dose, 5.0×10^{16} molecules/pulse); (star in solid circle) PV experiment on SC (medium dose, 9.0×10^{15} molecule/pulse); (solid right triangle) S ice. The dose for B, C_2, and S ice was 5.0×10^{16} molecules/pulse. The full line represents J_{ev}^{max} using P_{eq} from the literature.[43] Values of P_{eq} below 165 K have been extrapolated.

ice has the largest value of J_{ev} and k_c compared to the other types of ice studied in this work. In contrast, the lowest value of J_{ev}, paired with the lowest value of k_c is found for SC ice using a medium dose (9.0×10^{15} molecule/pulse) to probe the surface (Figures 4 and 9). In fact, J_{ev} for B ice is from 40 to 80% lower compared to C_2 ice which is outside of the present measurement uncertainty. J_{ev} for SC ice at the large dose of 5.0×10^{16} molecules/pulse is smaller by a factor of 2 at $T =$ 200 K and approximately 10% larger at $T = 175$ K compared to B ice. For other $H_2O(g)$ doses J_{ev} for SC ice changes as displayed in Figure 9 consistent with the dependence of γ on the dose shown in Figure 4. J_{ev} for S ice seems to match with the C_2 ice data set to within 20−50% in the range 165−202 K according to Figure 9. In summary, we obtain the sequence $J_{ev}(C_2) > J_{ev}(B) \approx J_{ev}(S) > J_{ev}(SC)$ in the range 150−210 K. In contrast to Chaix et al.[38] we obtain a γ value for C ice that is larger compared to B ice. This difference may perhaps be attributed to the conditions of deposition such as $H_2O(g)$ flow rate and temperature. However, we conclude in agreement with Chaix et al.[38] that SC ice presents a lower reactivity compared to B and C ice, probably owing to a low density of surface defects. Except for Chaix et al.,[38] no other work has been performed on both J_{ev} and γ while systematically varying the type of ice such as B, SC, and S. Consequently, comparisons with other results work are difficult. In agreement with the conclusion of Chaix et al.[38] the present work supports the conclusion that ices that present stress cracks and grain boundaries show larger values of J_{ev} and k_c.[20] However, the equilibrium vapor pressure is independent of the type of ice as will be discussed also below.

3.6. Annealing Studies on K Ice. At $T > 130$ K the cubic structure of K ice (I_c) should progressively convert to the hexagonal ice structure I_h.[38] As discussed by Davy and Somorjai[1] and Kumai,[36] K ice is transformed completely to I_h ice at $T > 173$ K after only 75 min. In the following experiment we have measured γ on K ice at 130 K using a $H_2O(g)$ pulse as a surface probe at a dose ranging from (0.15 to 8.0) $\times 10^{16}$ molecules/pulse. Subsequently, K ice was annealed to 150 K for 10 min before it was cooled to 130 K in order to measure γ once more. This is displayed in Figure 10 where γ obtained at the sample temperature of 130 K is plotted as a function of the annealing temperature. We note that for an annealing temperature of 150 K, γ decreases by 10% compared to fresh K ice. We observe a further decrease of γ with increasing annealing temperature. For an annealing temperature of 190 K, γ measured at 130 K decreases by 40% compared to fresh K ice. Similar results were observed by Chaix et al.[38] for D_2O ice and thus confirm the present results although the latter results for both γ and J_{ev} were slightly larger compared to the present values. For $T_{annealing} = 190$ K, γ of K ice is identical to γ obtained for C_3 ice measured at 140 or 150 K. A blank annealing run of C_3 ice deposited at 180 K and treated in an identical manner as K ice confirmed the thermodynamic stability of I_h ice under the present experimental conditions.. We conclude that metastable cubic ice I_c domains are irreversibly converted into I_h ice in the annealing process which assume the kinetic properties of C_3 ice after annealing. As showed in Appendix B, the negative T dependence is also observed on thermodynamically stable ice crystal phase I_h. If the T dependence is in the presence of metastable phase, we should observed a time-dependent value of k_c, which is not the case. Further details are discussed in Appendix B.

3.7. Thermochemical Parameters for C_2 Ice. Figure 11 presents an Arrhenius plot of k_c for C_2 ice which clearly displays two temperature regimes whose transition occurs at $T_{break} = 190 \pm 3$ K and leads to a high- and low-temperature regime for $T > 190$ K and $T < 190$ K, respectively. The slopes of the straight lines displayed in Figure 11 lead to a negative energy of activation for condensation $E_a^c = -4.1 \pm 1.4$ kcal/mol for $T > 190$ and $E_a^c = -0.18 \pm 0.14$ kcal/mol for $T < 190$ K. A

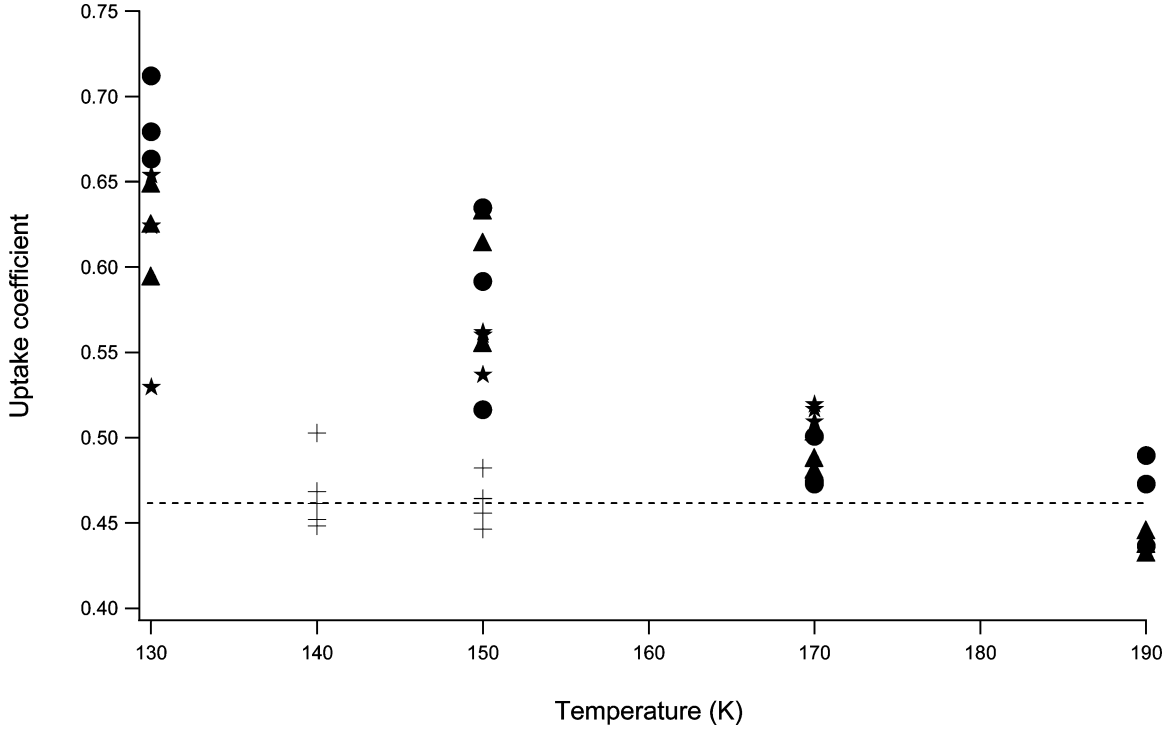

Figure 10. γ on K ice as a function of annealing temperature in comparison to γ of C_3 ice (+). Three different doses are used to probe the kinetics on K ice, namely, 1.5×10^{15} (★), 9.0×10^{15} (●), and 5.0×10^{16} (▲) molecules/pulse. The kinetic measurement was performed at 130 K for all substrates.

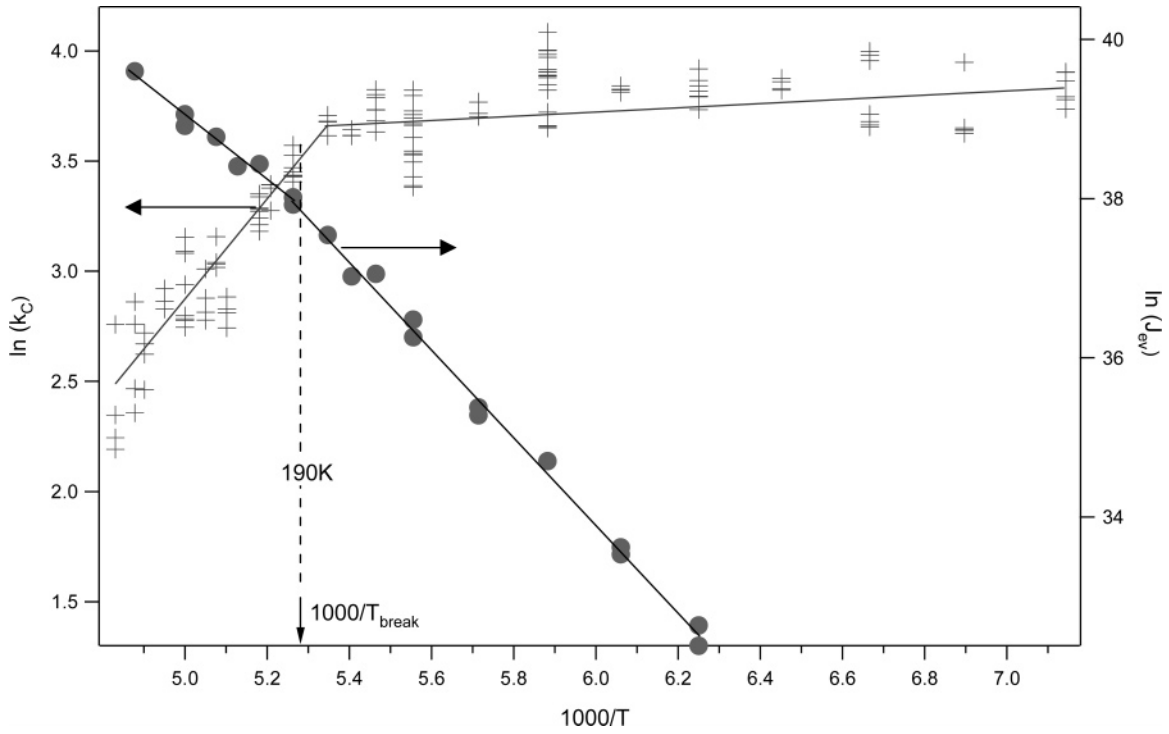

Figure 11. Arrhenius representation of k_c and J_{ev} for C_2 ice whose values are displayed in Table ESI-1 for J_{ev} and in Figure 3 for k_c. Two T regimes are apparent at the discontinuity $T_{break} = 190$ K. The activation energy for k_c at $T < 190$ K is $E_a^c = -0.18 \pm 0$ 0.14 and -4.1 ± 2.1 kcal mol^{-1} for $T > 190$ K and for J_{ev} 11.9 $\pm$ 1.3 and 7.9 $\pm$ 1.2 kcal mol^{-1}, respectively (Tables 4 and 5).

similar discontinuity in the Arrhenius plot of k_c has recently been observed for γ on C ice[42] at 193 K which is identical within experimental uncertainty to the break observed in this work. Delval and Rossi[42] obtained $E_a^c = -1.5 \pm 0.5$ and -0.3 ± 0.1 kcal/mol for $T > 190$ and $T < 190$ K, respectively. The change in the energy of activation E_a^c for C_2 ice at $T > 190$ K may be explained by a shift of the rate-limiting step with increasing T in the precursor mechanism that is discussed by Flückiger and Rossi.[39] As pointed out above, the merging of γ values at different $H_2O(g)$ doses for C ice at $T > 190$ K displayed in Figure 5 may have the same mechanistic origin in that the rate-limiting step in this T range is insensitive to the type of ice.

An additional way to characterize the ice surface from a kinetic point of view is to measure the energy of activation of evaporation E_a^{ev}. By plotting the J_{ev} data displayed in Figure 9 in an Arrhenius fashion, we obtain E_a^{ev} for C_2 ice. The J_{ev} data

TABLE 4: Energy of Activation E_a^c for Condensation of H_2O(g)

	E_a^c (kcal/mol)						
	Delval et al.[42]		Chaix et al.[38]		present work		
type of ice	193−223 K	182−193 K	190−220 K	140−190 K	$T \geq T_{break}$	$T < T_{break}$	T_{break} (K)
C_2	-1.5 ± 0.5	-0.3 ± 0.1	-4.2 ± 1	-0.24 ± 0.05	-4.1 ± 1.4	-0.18 ± 0.14	190 ± 3
B			-4.2 ± 1.7	-0.26 ± 0.13	-2.3 ± 0.9	-0.24 ± 0.11	185 ± 3
SC (L[a] dose)					-3.1 ± 0.6	-0.26 ± 0.15	170 ± 5
SC (M[a] dose)					-2.8 ± 0.8		no break
S					-0.3 ± 0.2		no break

[a] Key: L = large dose (5.0×10^{16} molecules/pulse); M = medium dose (9.0×10^{15} molecules/pulse).

TABLE 5: Energy of Activation E_a^{ev} for Evaporation of H_2O(g)

	E_a^c (kcal/mol)						
	Delval et al.[42]		Chaix et al.[38]		present work		
type of ice	193−223 K	173−193 K	190−220 K	140−190 K	$T \geq T_{break}$	$T < T_{break}$	T_{break} (K)
C_2	$+10.2 \pm 0.5$	$+12.0 \pm 0.5$			7.9 ± 1.2	11.9 ± 1.3	190 ± 3
B			$+8.3 \pm 1.0$	$+12.2 \pm 0.5$	9.9 ± 0.8	11.5 ± 1.0	185 ± 3
SC (L[a] dose)					8.5 ± 0.5	11.6 ± 0.8	170 ± 5
SC (M[a] dose)					9.5 ± 0.8		no break
S					11.5 ± 0.6		no break

[a] Key: L = large dose (5.0×10^{16} molecules/pulse); M = medium dose (9.0×10^{15} molecules/pulse).

TABLE 6: Enthalpy of Sublimation ΔH_s° of H_2O(g) from Ice Obtained from Tables 4 and 5

	E_a^c (kcal/mol)							
	Delval et al.[42]		Chaix et al.[38]		present work			
type of ice	193−223 K	182−193 K	190−220 K	140−190 K	$T \geq T_{break}$	$T < T_{break}$	entropy (cal K^{-1} mol^{-1}) $T > 190$ K	T_{break} (K)
C_2	11.7 ± 0.6	12.3 ± 0.5			12.0 ± 2.6	12.1 ± 1.5	34.6 ± 2.5	190 ± 3
B			12.5 ± 2.7	12.5 ± 0.6	12.2 ± 1.7	11.8 ± 1.1	29.8 ± 1.9	185 ± 3
SC (L[a] dose)					11.6 ± 1.1	11.9 ± 1.0	34.1 ± 2.1	170 ± 5
SC (M[a] dose)					12.3 ± 1.6		33.9 ± 2.4	no break
S					11.8 ± 0.8		33.6 ± 1.8	no break

[a] Key: L = large dose (5.0×10^{16} molecules/pulse); M = medium dose (9.0×10^{15} molecules/pulse).

also show a discontinuity at $T = 190 \pm 3$ K similar to k_c and are displayed in Figure 11 which shows that the break in k_c coincides with the one for J_{ev} at 190 K as it should. The data displayed in Figure 11 obtain $E_a^{ev} = 7.9 \pm 1.2$ for $T > 190$ K and $E_a^{ev} = 11.9 \pm 1.3$ kcal/mol for $T < 190$ K. In comparison with Delval and Rossi[42] who obtain $E_a^{ev} = 10.2 \pm 0.5$ and 12.0 ± 0.5 kcal/mol above and below 193 ± 3 K, respectively, we note a disagreement between the present E_a^{ev} value for $T > 190$ K. However, the large value $E_a^{ev} = 10.2$ kcal/mol of Delval and Rossi[42] is balanced by a correspondingly smaller negative activation energy for adsorption, $E_a^c = -1.5$ kcal/mol, to result in an enthalpy of sublimation identical to that obtained in this work as displayed in Tables 4, 5, and 6. The enthalpy of sublimation of H_2O(ice) from ice, ΔH_S°, is given by the difference in the activation energy for evaporation and condensation, $E_a^{ev} - E_a^c$. As displayed in Table 6, the value of ΔH_S° for C_2 ice for the high- and the low-temperature regime is equal to 12.0 ± 2.6 and 12.1 ± 1.5 kcal/mol, for $T > 190$ and $T < 190$ K, respectively, which is in excellent agreement with the accepted literature value for ice[47] of 12.2 kcal/mol. Moreover, Delval and Rossi[42] obtained 12.3 ± 0.5 and 11.7 ± 0.6 kcal/mol below and above 193 K, respectively, while Fraser et al.[45] obtained $\Delta H_S^\circ = E_a^{ev} = 11.5$ kcal/mol for $T < 193$ K. This latter low value for ΔH_S may in part be explained by the fact that E_a^c was arbitrarily set to zero. Fortunately, this assumption does not have a large effect on ΔH_S° in the low T range where only a small negative value for E_a^c is observed. The present results clearly demonstrate that the assumption $E_a^c = 0$ at $T > 190$ K would clearly lead to an erroneous, that is lower, value of ΔH_S° in that T range in comparison with the accepted literature values. This work is in agreement with the results of Delval and Rossi[42] who claimed that the sole measurement of E_a^{ev} in general is not sufficient for the determination of ΔH_S° in conjunction with the assumption $E_a^c = 0$. Haynes et al.[40] and Davy and Somorjai[1] obtained 11.8 ± 0.2 and 12.2 kcal/mol for ΔH_S° of H_2O(ice) ice, respectively, both of which are in agreement with the accepted literature value of Jancso et al.[47] Sack and Baragiola[46] who also assummed $E_a^c = 0$ and obtained 0.45 eV/molecule which corresponds to 10.3 ± 0.7 kcal/mol at $T < 190$ K is significantly lower than the accepted literature value. The kinetic and thermodynamic parameters for E_a^c, E_a^{ev}, and ΔH_S° are all displayed in Tables 4−6, respectively, to summarize and facilitate a critical comparison. The entropy of sublimation for C_2 ice was $\Delta S_S = 34.6 \pm 2.5$ cal K^{-1} mol^{-1}, which is in fair agreement with the value of 31.0 cal K^{-1} mol^{-1} measured by Haynes et al.[40]

3.8. Thermochemical Parameters for Other Types of Ice. The energies of activation E_a^c and E_a^{ev} for the other investigated types of ice have been obtained from the T dependence of J_{ev} and k_c and are listed in Tables 4−6 together with T_{break}, the temperature of transition in the Arrhenius plot of ln k_c or ln J_{ev} vs $1000/T$. Taking B ice as an example, we obtained $E_a^c = -2.3 \pm 0.9$ and -0.24 ± 0.11 kcal/mol in the range 185−210 K and in the range 160−185 K, respectively. The enthalpy of sublimation ΔH_S° for B ice is identical to that of C_2 ice within experimental uncertainty with $\Delta H_S^\circ = 12.2 \pm 1.7$ kcal/mol for γ values at $T > 185$ K and $\Delta H_S^\circ = 11.8 \pm 1.1$ kcal/mol at $T < 185$ K. Chaix et al.[38] obtained 12.5 ± 2.7 for the high-

temoerature regime and 12.5 ± 0.6 kcal/mol for the low-temperature regime (Table 6) with T_{break} measured at 190 K for $\Delta H_S°$ on $D_2{}^{16}O$(ice) B ice. The kinetic parameters ($E_a{}^c$, $E_a{}^{ev}$) of Chaix et al.[38] are remarkably similar to the present values as displayed in Tables 4 and 5 including the value of $T_{break} = 190$ K for C_2 ice.

For a large H_2O(g) dose interacting with SC ice $E_a{}^c = -3.1 \pm 0.6$, $E_a{}^{ev} = 8.5 \pm 0.5$ kcal/mol in the range 170−205 K whereas $E_a{}^c = -0.26 \pm 0.15$, $E_a{}^{ev} = 11.6 \pm 0.8$ kcal/mol was measured between 145 and 170 K as displayed in Tables 4 and 5. For the medium and small doses of H_2O(g) interacting with SC ice, the temperature range is not sufficiently large to draw conclusions on the location of T_{break}. The related energy of sublimation $\Delta H_S°$ for the large H_2O(g) dose is equal to 11.6 ± 1.1 kcal/mol in the high-temperature range $T > 170$ K and to 11.9 ± 1.0 kcal/mol in the low-temperature range $T < 170$ K. $\Delta H_S°$ was calculated as 12.3 ± 1.6 kcal/mol for the medium dose on SC ice obtained across the full T range. Because $E_a{}^c$ is close to zero on S ice, namely, −0.3 ± 0.2 kcal/mol, $E_a{}^{ev}$ must be close to $\Delta H_S°$, which we evaluated as $E_a{}^{ev} = 11.5 \pm 0.6$ leading to $\Delta H_S° = 11.8 \pm 0.8$ kcal/mol. This value is in agreement with $\Delta H_S°$ calculated for C_2, B, and SC ice within the uncertainty of the measurement. The results of Table 6 reveal that $\Delta H_S°$ is identical within the uncertainty of the data for the different types of ice. We also found that for C, B, and SC ice there is a discontinuity in the Arrhenius plot of k_c or γ at T_{break}. However, T_{break} does not occur at the same temperature for the three mentioned types of ice. This may be explained by the fact that the change in the rate-limiting step in the precursor mechanism is a function of the type of ice.

To interpret the condensation of H_2O(g) on ice, we use the Langmuir ansatz expressed in reaction 6[38]

$$SS + H_2O(g) \underset{k_2}{\overset{k_1}{\rightleftharpoons}} H_2O(ads) \underset{k_4}{\overset{k_3}{\rightleftharpoons}} SS + H_2O(ice) \qquad (6)$$

where SS is a free surface site. H_2O(ads) and H_2O(ice) correspond to the precursor species responsible for the negative temperature dependence of k_c or γ and the thermodynamically stable bulk I_h ice H_2O(ice), respectively.

Results from chemical-kinetic modeling[38,39] indicate that k_1 depends on the type of ice whereas the values k_2, k_3, and k_4 strongly depend on T but not on the type of ice. By use of the enthalpy diagram of Flückiger et al.[39] for the present case of H_2O(g) adsorption, k_3 is rate-limiting for H_2O(g) uptake on ice at $T < T_{break}$, that is, $k_3 < k_2$ and H_2O desorption from H_2O(ads) is not important at these low temperatures. At $T \geq T_{break}$, k_2 increasingly becomes larger than k_3 so that the desorption of H_2O(ads) from the precursor state k_2 is faster compared to rearrangement of H_2O(ads) into H_2O(ice), process 3. Conversely, J_{ev} at $T < T_{break}$ is controlled by k_4, that is, $k_4[SS] \ll k_2$, whereas for $T \geq T_{break}$ k_3 significantly increases such that a fraction of H_2O(ads) predestined for evaporation in process 2 returns to H_2O(ice) via rearrangement process 3. The non-Arrhenius behavior of both k_c and $J_{ev}(R_{ev})$ displayed in Figure 11 is thus rooted in the unequal T dependences of the rate coefficients k_1 to k_4.

In fact, Tables 4 and 5 show that the individual values of T_{break} for both J_{ev} and k_c coincide within experimental uncertainty. This is a necessary requirement for the thermochemical closure of the condensation/evaporation kinetics discussed below.

3.9. The Equilibrium Vapor Pressure P_{eq} as a Thermodynamic Constraint for Chemical Kinetics. We have calculated the vapor pressure P_{eq} of water vapor in equilibrium with water ice using both J_{ev} or R_{ev} and k_c, which were separately determined for the different types of ice as explained in the previous sections. The measured equilibrium vapor pressure P_{eq} is calculated using eq 7 in order to check if the different types of ice (C, B, SC, and S) significantly differ in P_{eq} at a given temperature. The calculation of P_{eq} makes use of the measured value of k_c, F_{ev}, and T_S, the temperature of the ice substrate, and serves as a powerful thermodynamic constraint for the internal consistency of the measured kinetic parameters.

$$P_{eq} = \frac{F_{ev} R T_S}{k_c V} \text{ [Torr]} \qquad (7)$$

Because the sample and the reactor temperature are different, k_c has been corrected for this temperature difference as shown by Delval and Rossi.[34] As an example for the magnitude of this correction, one obtains P_{eq} values smaller by 23 and 18% at 180 and 200 K, respectively, using the corrected k_c in eq 7 compared to the uncorrected one. To observe a trend in the equilibrium vapor pressure for the different types of ice, P_{eq} was plotted as a function of T in Figure 12 using data from Tables ESI-1 to ESI-7 that exibit the complete data for J_{ev} and P_{eq}.

Most P_{eq} values are comprised in the stated uncertainty range according to the $1/e$ criterion. The largest deviation at the end of the low T measurement range is approximately 100% at $T =$ 150 K for B ice, which is the lowest value of P_{eq} that could be measured. We conclude that the P_{eq} values are identical for all the different types of ice investigated despite the individual differences in R_{ev} and k_c values. Both will change to the same extent in order to keep $[H_2O(g)]_{eq}$ or P_{eq} constant at a given T for all ices. The present results indicate that P_{eq} measured in the present work is in general larger by a factor of 1.83 ± 0.20 in comparison to the results of Haynes et al.[40] As an example, they obtained $P_{eq} = 6.0 \times 10^{-6}$ Torr at 175 K while the present work leads to $P_{eq} = 1.1 \times 10^{-5}$ Torr for C_1 ice. According to eq 7, this is consistent with the fact that J_{ev} of Haynes et al.[40] is identical to the present work whereas their γ (or k_c) value ($\gamma = 0.67$ at 175 K) is larger by a factor of 1.76 in comparison to the present work.

The full and dashed lines drawn in Figure 12 represent P_{eq} given by Marti and Mauersberger[43] between 169 and 240 K and by Mauersberger and Krankowsky[48] in the range 164.5−169 K, respectively. P_{eq} values from these two references seem to be larger compared to those measured in this work by approximately 50%. This difference is consistent within the uncertainty of the present results as displayed by the typical uncertainty limits given in Figure 12. We therefore conclude that our P_{eq} values are identical to those measured by Mauersberger and co-workers within the stated uncertainty limits.

4. Atmospheric Implications and Conclusions

The measured γ values for $T > 205$ K displayed for C ice in Figures 3 and 5 are found to be systematically low compared to values obtained using a stirred flow reactor where the partial pressure of H_2O(g) is larger compared to results obtained under molecular flow conditions such as used in this work.[42] The γ values for $D_2{}^{18}O$(g) vapor interacting with $D_2{}^{16}O$(ice) ice obtained by Chaix et al.[38] also dropped precipitously in the range 205−219 K to result in a systematic low bias. In contrast, the above-referenced γ values of Delval and Rossi[42] extend up to 240 K without extensive decrease at the high T end. It seems plausible to attribute this drooping of γ obtained in the present

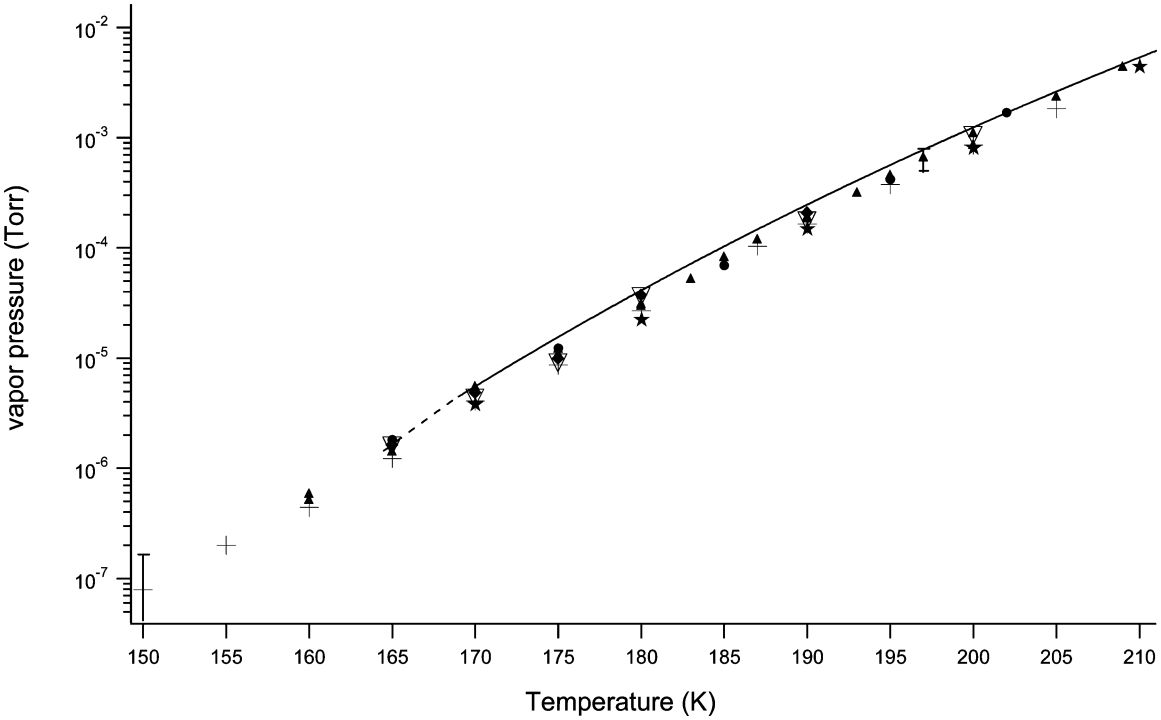

Figure 12. Equilibrium H_2O(g) vapor pressure P_{eq} measured using forward and backward rates obtained from the PV technique for difference types of ice. Data labeled (▲), (+), (♦), (▽), and (●) correspond to C, B, SC (large dose), SC (medium dose), and S ice, respectively. The (★) symbol represents P_{eq} measured by the CFM experiment (Appendix A). The full and the dashed lines represent the results of Marti and Mauersberger[43] and Mauersberger and Krankowsky,[48] respectively. The uncertainty displayed at 197 K serves as an illustration of the typical uncertainty.

study under molecular flow conditions to an unexpected change of the evaporation rather than to the condensation rate. It appears that the evaporation rate or flux, R_{ev} or J_{ev}, unduly increases with temperature above 205 K thereby effectively decreasing the measured γ value despite our ability to separate both rate processes. Because this effect takes place at the high-temperature end of the range corresponding to a reduced surface residence time compared to the low-temperature end, we attribute this increase in J_{ev} to possible incomplete energy accommodation of the H_2O−ice adsorbate or precursor state on the ice surface. One has to remember that in the present experiment H_2O(g) vapor at ambient temperature collides with an ice surface at a given low T and that energy accommodation must occur prior to evaporation. This incomplete thermalization process of the H_2O(ads) precursor state on the surface may be compared to chemical activation for gas-phase processes. Because Delval and Rossi[42] performed their study at higher total pressure, corresponding to stirred flow conditions, the degree of thermalization of the adsorbed H_2O(ads) precursor is expected to be higher on account of the increased number of collisions.

The time, t_{ev}, to complete evaporation of an ice particle of radius r at a given relative humidity (RH) is given in eq 8

$$t_{ev} = \frac{\left(\frac{\rho N_L}{M}\right)^{2/3}\left(\frac{r}{a}\right)}{J_{ev}(1 - RH)} \tag{8}$$

where ρ is the density of ice, $M = 18$ g mol^{-1} for H_2O, r is the ice particle radius, and a is the distance between two layers of H_2O(ice) in ice.[20] Equation 8 is based on layer-by-layer evaporation of H_2O(ice) of a spherical ice particle following a zero-order rate law. For RH = 80%, $J_{ev} = 10^{17}$ molecules s^{-1} cm^{-2}, and $a = 4 \times 10^{-8}$ cm, we obtain $t_{ev} = 125$ s, which is a lower limit to the true evaporation time owing to the competition of mass transfer and heterogeneous chemistry whose rate constants k_{diff} and k_c are given in eqs 9 and 10

$$k_{diff} = 4\pi r_0 D N_0 \tag{9}$$

$$k_c = \frac{\bar{c}}{4}\gamma(S/V) \tag{10}$$

D, N, and (S/V) correspond to the diffusion coefficient of H_2O(g)/atmosphere of air (∼0.1 cm^2 s^{-1}), N to the ice particle number density (particles cm^{-3}), and (S/V) to the surface area density (cm^2 cm^{-3}) using $N_0 4\pi r_0^2 = (S/V)$ as a constraining condition.

The overall rate constant $k_{tot} = k_c k_{diff}/(k_c + k_{diff})$ is calculated to be 7.1×10^{-4} s^{-1} with $k_{diff} = 1.0 \times 10^{-3}$ s^{-1} and $k_c = 2.4 \times 10^{-3}$ s^{-1} using $(S/V) = 10^{-6}$ cm^2 cm^{-3} and $r = 1$ μm. Thermodynamic closure requires that both k_c and J_{ev} are slowed by diffusion to the same extent. This leads to a factor of $2.4 \times 10^{-3}/7.1 \times 10^{-4} = 3.4$ by which J_{ev} is slowed at atmospheric pressure compared to molecular flow conditions. This leads to an improved estimate for t_{ev} of 425 s or approximately 7 min. It behooves us to point out that t_{ev} for large ice particles is entirely characterized by gas-phase diffusion of H_2O(g) toward the ice particle and that therefore the overall rate constant k_{tot} is only marginally affected by k_c or γ.

The four messages resulting from this work that are important for atmospheric applications are the following:

(a) The uptake coefficient γ is significantly less than unity for $T > 130$ K. This decrease compared to the theoretical maximum amounts to approximately an order of magnitude for C ice at 200 K. The identical decrease applies also for the corresponding J_{ev} values compared to their theoretical maximum value J_{ev}^{max} owing to thermochemical constraints. The largest γ value was measured on K ice at 130 K and led to $\gamma = 0.64 \pm 0.05$. For B and C ice, γ ranged from 0.35 ± 0.02 to 0.10 ± 0.02 and 0.48 ± 0.04 to 0.08 ± 0.03 in the range 140−210 K, respectively. On S ice γ is between 0.32 ± 0.05 and $0.29 \pm$

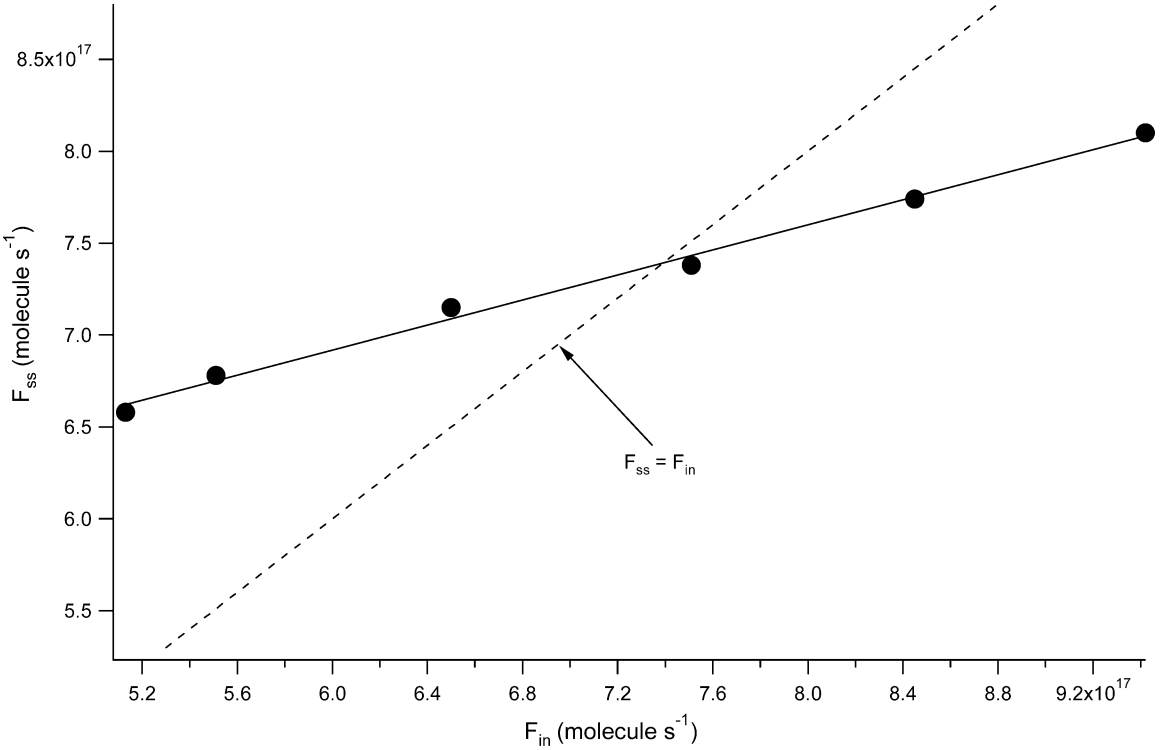

Figure 13. F_{ss} as a function of F_{in} in the measurement of J_{ev} and k_c for B ice at 200 K using the 14 mm aperture.

0.02 in the range 136−200 K while for SC ice γ lies between 0.38 ± 0.01 and 0.057 ± 0.007 in the range 145−205 K.

(b) The kinetic parameters (J_{ev}, k_c) depend on the type of ice for each type of ice investigated whereas the thermodynamic parameters ($\Delta H°_{sub}$, ΔS_{sub}) are independent of the type of ice within experimental uncertainty.

(c) The molecular mechanism for adsorption/desorption of H_2O(g) vapor over ice is complex as evident from the negative temperature dependence of k_c. In contrast to previous work, additional details have been discovered in terms of a change in slope in both $k_c(T)$ and $J_{ev}(T)$ when k_c is represented in Arrhenius form. This "break" in slope occurs in the range (170−190) ± 5 K depending on the type of ice and is related to the fact that the relative importance of k_2 and k_3 in the detailed chemical kinetic mechanism is increasing with increasing T.

(d) The rate of adsorption k_1 in the complex mechanism depends on the defect structure or, more generally, on structural parameters of the ice sample. The colliding H_2O(g) molecule has to search for an active site on the ice to enable the formation of the precursor state consistent with Langmuir ansatz. Therefore, k_1 depends on the type of ice whereas the remaining parameters k_2, k_3, and k_4 do not within the uncertainty of the data. However, the latter rate constants strongly depend on T in contrast to k_1.

In conclusion, the kinetic data collected in this investigation should encourage workers in the field to obtain well-characterized atmospheric ice samples that may be compared to the surrogate ices investigated in the present study.

Acknowledgment. Generous support of this research was granted by OFES (Office Fédéral de l'enseignement et de la science) in the framework of the EU projects CUTICE and THALOZ.

Appendix A

Additional Experiments. CFM and TASSM: Two Alternative Steady-State Experiments. To measure J_{ev}, we have used two additional, albeit different steady-state methods, namely, the compensated flow method (CFM) and the two-aperture steady-state method (TASSM) with the goal to compare results of both k_c and J_{ev} obtained from steady-state and transient (PV) methods. B ice samples have been used for the confirmation of the present PV results on J_{ev} displayed in Figure 9 and Table ESI-6.

The general way to perform a CFM experiment is to measure the H_2O(g) flow, $F_{ss} = V[H_2O]k_{esc}$, escaping from the flow reactor as a function of an additional measured H_2O(g) flow, namely, F_{in}, in the presence of ice. The mass balance is expressed in eq A-1 which leads to eq A-2 after rearrangement

$$F_{in} + F_{ev} = F_{ss} + V[H_2O(g)]k_c \qquad \text{(A-1)}$$

$$F_{ss} = \frac{F_{ev}}{1 + \frac{k_c}{k_{esc}}} + \frac{F_{in}}{1 + \frac{k_c}{k_{esc}}} \qquad \text{(A-2)}$$

where $F_{ev}/(1 + (k_c/k_{esc}))$ and $1/(1 + (k_c/k_{esc}))$ are the intercept and slope of the straight line of a plot of $F_{ss}(F_{in})$, respectively.

For the special case of $F_{in} = F_{ss,}$ J_{ev} may be evaluated from eq A-3

$$J_{ev} = \frac{F_{ev}}{A_S} = \frac{k_c}{k_{esc}} \frac{F_{ss}}{A_S} \qquad \text{(A-3)}$$

In this case the flow rate F_{in} is chosen in such a way so as to exactly match F_{ss}, in the presence of the ice sample. To calculate J_{ev} using eq A-3, we use k_c measured on B ice using a PV experiment (Table ESI-2). All CFM data on H_2O interacting with B ice are summarized in Table ESI-6.

A more general approach to measure both J_{ev} and k_c is to plot F_{ss} as a function of F_{in} and dividing the intercept by the slope of the straight line expressed in eq A-2. An example of such a plot is shown in Figure 13 where the measurement was performed on B ice held at 200 K. In a PV experiment F_{ev} was

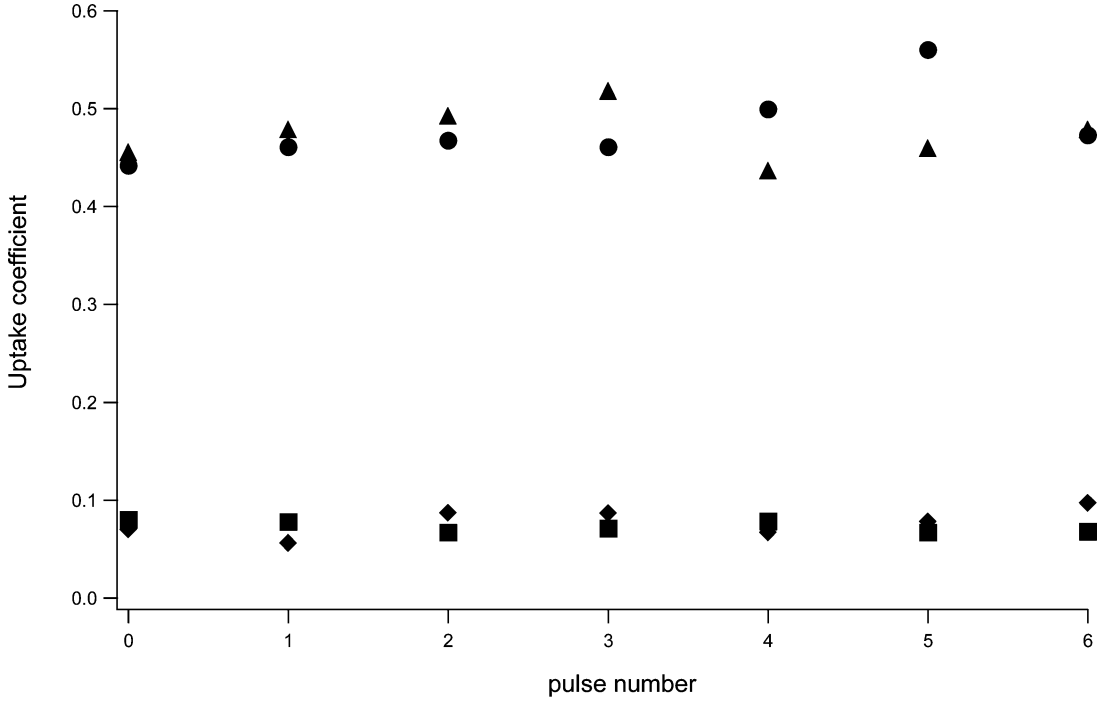

Figure 14. Repetitive pulse experiment (RPE) on C_2 ice. The uptake coefficient γ is plotted as a function of the pulse event for different pulse frequencies and temperature. The (▲) and the (●) data points were obtained at 170 K at frequencies of 1 and 3 Hz, respectively. The (■) and the (◆) results were obtained at 210 K at frequencies of 1 and 3 Hz, respectively. The dose used to measure γ was 5.0×10^{16} molecules/pulse.

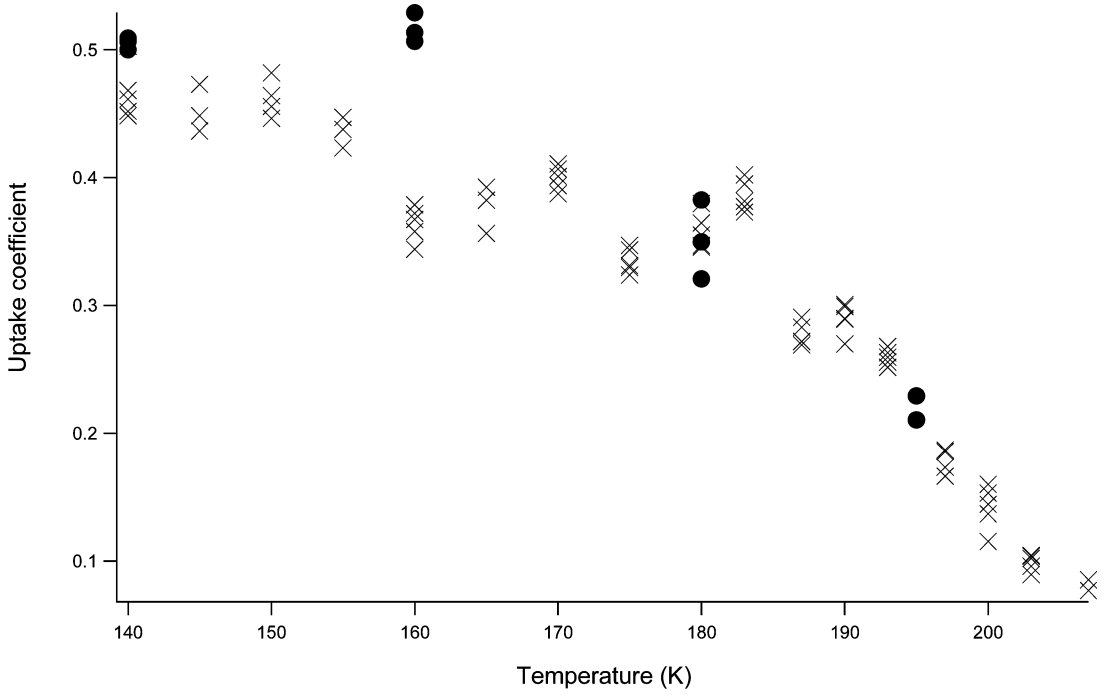

Figure 15. Uptake coefficient γ on C_1 ice for fresh (×) and annealed (●) ice as a function of T. The ice surface was annealed at 220 K for 10 min prior to the PV measurement.

calculated to be 1.4×10^{18} molecules s^{-1} leading to $J_{ev} = (7.9 \pm 1.1) \times 10^{16}$ molecules cm^{-2} s^{-1} and $k_c = 13.8 \pm 1.7$ s^{-1}. The knowledge of both the slope and intercept of the straight line $F_{ss}(F_{in})$ leads to the separate determination of F_{ev} or J_{ev} and k_c, namely, $J_{ev} = (6.8 \pm 1.9) \times 10^{16}$ molecules cm^{-2} s^{-1} and $k_c = 16.3 \pm 4.1$ s^{-1}. We conclude that the PV and CFM experiments are in good agreement within experimental uncertainty. For all results displayed in Table ESI-6, the kinetics was calculated by using eq A-3 ($F_{in} = F_{out}$) where $F_{in} = F_{ss}$ was chosen by trial and error for B ice at 200 K.

The second technique, TASSM, uses two or more independent data sets of F_{ss} and k_{esc} by choosing two or more escape apertures (14 and 8 mm) and measuring the corresponding value of F_{ss}. Using eq 4, we obtain two independent sets of equations to be solved for F_{ev} and k_c. The solution for F_{ev} and k_c is given in eq A-4

$$F_{ev} = \frac{F_{ss}(L)(k_{esc}(L) - k_{esc}(S))}{k_{esc}(L) - rk_{esc}(S)} \qquad \text{(A-4)}$$

and

$$k_c = \frac{(r-1)k_{esc}(S)k_{esc}(L)}{k_{esc}(L) - rk_{esc}(S)}$$

with

$$r = F_{ss}(L)/F_{ss}(S)$$

where L and S are related to the large (L) and small (S) escape aperture, respectively.

By measuring $F_{ss}(L)$, $F_{ss}(S)$, at known values of $k_{esc}(L)$ and $k_{esc}(S)$ for B ice at different temperatures, we obtain F_{ev} and k_c. All experimental data for TASSM are summarized in Table ESI-7. Unfortunately, this method is more sensitive to experimental uncertainties due to the subtraction of two similar values in the denominator as may be seen from eq A-4. This leads to a large uncertainty for both k_c and F_{ev}.

To show that a PV experiment of H_2O vapor interacting with ice does not affect J_{ev} in the aftermath of a H_2O(g) pulse, both CFM and TASSM experiments have been performed on B ice as both are essentially steady-state experiments. J_{ev} on B (▼) ice using CFM matched that measured using the PV (×) technique, within 15%, except for 175 K and is displayed in Figure 9.

In addition, we have performed repetitive pulse experiments (RPEs) of H_2O(g) interacting with C_2 ice at 170 and at 210 K at different pulse frequencies in order to test if k_c changes on the time scale of the present experiments or if there are measurable memory effects on the ice substrate originating from previous probe pulses. We have summarized the results of this experiment in Figure 14 where γ is plotted as a function of the number of pulse events, at two temperatures and pulse frequencies using a dose of 5×10^{16} molecules/pulse. These experiments tell us that the pulse decay rate constant is independent of the number of previous pulses and therefore does not affect the measured kinetics at low and high temperature. We conclude that there is no measurable difference at both 210 and 170 K for the two chosen pulse frequencies of 1 and 3 s^{-1}. Similarly, Haynes et al.[40] concluded that an additional flow of H_2O(g) perturbs neither the evaporation nor the condensation of H_2O-(g) on ice.

Appendix B

To ascertain that C ice preserves the hexagonal I_h ice structure under annealing, we first deposited C_1 ice at $T = 180$ K, which is under conditions that result in the formation of ice with I_h structure, cooled it subsequently to 140 K, and measured k_c using the PV technique. By increasing the annealing temperature and measuring γ, we obtain the kinetic data with the (×) label of Figure 15. We annealed the surface to 220 K for 10 min before lowering it to 140 K in order to perform a second set of measurements labeled with the (●) symbol. In Figure 15, the crosses and the circle symbols therefore describe the γ values measured before and after annealing to 220 K, respectively. Before each temperature change, 10 min was allowed before performing measurement to obtain ice temperature homogeneity. The first γ was measured at 140 K (×) while T was increased sequentially to reach 209 K after approximately 160 min. After the annealing at 220 K, T was decreased at 140 K and $\gamma(T)$ was measured subsequently at 140, 160, 180, and 195 K in 40 min. There is no significant difference between k_c obtained before and after the annealing process for hexagonal C ice I_h for the duration of the experiment (over 200 min) as displayed in Figure 15.[36,38] This leads to the conclusion that the non-Arrhenius behavior of k_c at T_{break} is related to the chemical−kinetic mechanism displayed in reaction 6 as opposed to a phase transition.

Supporting Information Available: Tables of condensation rate constants, evaporation rates, and equilibrium vapor pressures for C_2, B, SC, and S ice and figure showing uptake coefficient of H_2O(g) as a function of temperature. This material is available free of charge via the Internet at http://pubs.acs.org.

References and Notes

(1) Davy, J. G.; Somorjai, G. A. *J. Chem. Phys.* **1971**, *55*, 3624.
(2) Intergovernmental Panel on Climate Change (IPCC). http://www-.grida.no/climate/ipcc_tar/.
(3) Shaw, R. A. *J. Atmos. Sci.* **2000**, *57*, 3452.
(4) Spichtinger, P.; Gierens, K.; Smit, H. G. J.; Ovarlez, J.; Gayet, J. F. *Atmos. Chem. Phys.* **2004**, *4*, 639.
(5) Shine, K. P.; Sinha, A. *Nature* **1991**, *354*, 382.
(6) Jensen, E. J.; Toon, O. B.; Vay, S. A.; Ovarlez, J.; May, R.; Bui, T. P.; Twohy, C. H.; Gandrud, B. W.; Pueschel, R. F.; Schumann, U. *J. Geophys. Res.*, [*Atmos.*] **2001**, *106*, 17253.
(7) Gierens, K.; Brinkop, S. *Theor. Appl. Climatol.* **2002**, *71*, 129.
(8) Gierens, K.; Spichtinger, P. *Ann. Geophys.* **2000**, *18*, 499.
(9) Gibson, G. G.; Wielicki, B. A. *CERES Interdisciplinary Science Principal Investigator, NASA Langley Reasearch Center (LaRC)*, http://asd-www.larc.nasa.gov/ceres/ASDceres.html.
(10) Gierens, K.; Schumann, U.; Helten, M.; Smit, H.; Wang, P. H. *J. Geophys. Res.*, [*Atmos.*] **2000**, *105*, 22743.
(11) Penner, J. E. *Intergouvernment Panel on Climat Change. Working Group, I.*; *Intergouvernmental Panel on Climate Change. Working Group III. Aviation and the global atmosphere: a special repport of IPCC Working Groups I and III in collaboration with the scientific Assessment Panel to the Montreal Protocol on Substances that Deplete the Ozone Layer*; Cambridge University Press: Cambridge, 1999.
(12) Eremenko, M. N.; Zasetsky, A. Y.; Boone, C. D.; Sloan, J. J. *Geophys. Res. Lett.* **2005**, *32*.
(13) Parungo, F. *Atmos. Res.* **1995**, *38*, 249.
(14) Jensen, E. J.; Kinne, S.; Toon, O. B. *Geophys. Res. Lett.* **1994**, *21*, 2023.
(15) Borrmann, S.; Solomon, S.; Dye, J. E.; Luo, B. P. *Geophys. Res. Lett.* **1996**, *23*, 2133.
(16) Zerefos, C. S.; Eleftheratos, K.; Balis, D. S.; Zanis, P.; Tselioudis, G.; Meleti, C. *Atmos. Chem. Phys.* **2003**, *3*, 1633.
(17) Solomon, S.; Garcia, R. R.; Rowland, F. S.; Wuebbles, D. J. *Nature* **1986**, *321*, 755.
(18) Libbrecht, K. G. *Rep. Prog. Phys.* **2005**, *68*, 855.
(19) Young, K. C. Oxford University Press: New York, 1993.
(20) Hobbs, P. V. *Ice Physics*; Oxford University Press: Oxford; 1969; p 397.
(21) Murphy, D. M. *Geophys. Res. Lett.* **2003**, *30*, DIO: 10.1029/2003GL018566.
(22) Whalley, E. S. *Science* **1981**, *211*, 389.
(23) Murray, J. B.; Knopf, A. D.; Bertram, K. A. *Nature* **2005**, *434*, 202.
(24) Bonacci, J. C.; Myers, A. L.; Nongbri, G.; Eagleton, L. C. *Chem. Eng. Sci.* **1976**, *31*, 609.
(25) Chodes, N.; Warner, J.; Gagin, A. *J. Atmos. Sci.* **1974**, *31*, 1351.
(26) Koros, R. M.; Deckers, J. M.; Andres, R. P.; Boudart, M. *Chem. Eng. Sci.* **1966**, *21*, 941.
(27) Kramers, H.; Stemerding, S. *Appl. Sci. Res., Sect. A* **1951**, *3*, 73.
(28) Nabavian, K.; Bromley, L. A. *Chem. Eng. Sci.* **1963**, *18*, 651.
(29) Isono, K.; Iwai, K. *Nature* **1969**, *223*, 1149.
(30) Leu, M. *Geophys. Res. Lett.* **1988**, *15*, 17.
(31) Sinnarwalla, A. M.; Alofs, D. J.; Carstens, J. C. *J. Atmos. Sci.* **1975**, *32*, 592.
(32) Schulze, F. W.; Cammenga, H. K. *Ber. Bunsen-Ges. Phys. Chem. Chem. Phys.* **1980**, *84*, 163.
(33) Caloz, F.; Fenter, F. F.; Tabor, K. D.; Rossi, M. J. *Rev. Sci. Instrum.* **1997**, *68*, 3172.
(34) Delval, C.; Fluckiger, B.; Rossi, M. J. *Atmos. Chem. Phys.* **2003**, *3*, 1131.
(35) Fenter, F. F.; Caloz, F.; Rossi, M. J. *Rev. Sci. Instrum.* **1997**, *68*, 3180.
(36) Kumai, M. *J. Glaciol.* **1967**, *7*, 95.
(37) Knight, C. A. *J. Glaciol.* **1996**, *42*, 585.
(38) Chaix, L.; van den Bergh, H.; Rossi, M. J. *J. Phys. Chem. A* **1998**, *102*, 10300.
(39) Fluckiger, B.; Rossi, M. J. *J. Phys. Chem. A* **2003**, *107*, 4103.

(40) Haynes, D. R.; Tro, N. J.; George, S. M. *J. Phys. Chem.* **1992**, *96*, 8502.
(41) Brown, D. E.; George, S. M.; Huang, C.; Wong, E. K. L.; Rider, K. B.; Smith, R. S.; Kay, B. D. *J. Phys. Chem.* **1996**, *100*, 4988.
(42) Delval, C.; Rossi, M. J. *Phys. Chem. Chem. Phys.* **2004**, *6*, 4665.
(43) Marti, J.; Mauersberger, K. *Geophys. Res. Lett.* **1993**, *20*, 363.
(44) Smith, J. A.; Livingston, F. E.; George, S. M. *J. Phys. Chem. B* **2003**, *107*, 3871.
(45) Fraser, H. J.; Collings, M. P.; McCoustra, M. R. S.; Williams, D. A. *Mon. Not. R. Astron. Soc.* **2001**, *327*, 1165.
(46) Sack, N. J.; Baragiola, R. A. *Phys. Rev. B* **1993**, *48*, 9973.
(47) Jancso, G.; Pupezin, J.; Vanhook, W. A. *J. Phys. Chem.* **1970**, *74*, 2984.
(48) Mauersberger, K.; Krankowsky, D. *Geophys. Res. Lett.* **2003**, *30*, 1121.